J. Fluid Mech. (1994), *vol.* 271, *pp.* 119–151

Linear dynamics of wind waves in coupled turbulent air–water flow. Part 1. Theory

By S. E. BELCHER[1]†, J. A. HARRIS[2]‡ AND R. L. STREET[2]

[1]Department of Applied Mathematics and Theoretical Physics, University of Cambridge, Silver Street, Cambridge CB3 9EW, UK

[2]Environmental Fluid Mechanics Laboratory, Stanford University, Stanford, CA 94305-4020, USA

(Received 8 October 1993 and in revised form 25 January 1994)

When air blows over water the wind exerts a stress at the interface thereby inducing in the water a sheared turbulent drift current. We present scaling arguments showing that, if a wind suddenly starts blowing, then the sheared drift current grows in depth on a timescale that is larger than the wave period, but smaller than a timescale for wave growth. This argument suggests that the drift current can influence growth of waves of wavelength λ that travel parallel to the wind at speed c.

In narrow 'inner' regions either side of the interface, turbulence in the air and water flows is close to local equilibrium; whereas above and below, in 'outer' regions, the wave alters the turbulence through rapid distortion. The depth scale, l_a, of the inner region in the air flow increases with c/u_{*a} (u_{*a} is the unperturbed friction velocity in the wind). And so we classify the flow into different regimes according to the ratio l_a/λ. We show that different turbulence models are appropriate for the different flow regimes.

When $(u_{*a}+c)/U_B(\lambda) \ll 1$ ($U_B(z)$ is the unperturbed wind speed) l_a is much smaller than λ. In this limit, asymptotic solutions are constructed for the fully coupled turbulent flows in the air and water, thereby extending previous analyses of flow over irrotational water waves. The solutions show that, as in calculations of flow over irrotational waves, the air flow is asymmetrically displaced around the wave by a non-separated sheltering effect, which tends to make the waves grow. But coupling the air flow perturbations to the turbulent flow in the water reduces the growth rate of the waves by a factor of about two. This reduction is caused by two distinct mechanisms. Firstly, wave growth is inhibited because the turbulent water flow is also asymmetrically displaced around the wave by non-separated sheltering. According to our model, this first effect is numerically small, but much larger erroneous values can be obtained if the rapid-distortion mechanism is not accounted for in the outer region of the water flow. (For example, we show that if the mixing-length model is used in the outer region all waves decay!) Secondly, non-separated sheltering in the air flow (and hence the wave growth rate) is reduced by the additional perturbations needed to satisfy the boundary condition that shear stress is continuous across the interface.

† Present address: Department of Meteorology, University of Reading, Reading RG6 2AU, UK

‡ Present address: G.K.Williams Cooperative Research Centre, Department of Chemical Engineering, The University of Melbourne, Parkville, Victoria, 3052, Australia.

In a companion paper, we develop a numerical model for the coupled air–water flow with waves of arbitrary speed and in another we examine the detailed energy budget of the wave motions.

1. Introduction

How does the wind generate ocean waves, and how do these waves evolve? For many years these questions have been studied using a variety of techniques. Yet the large body of literature currently available tends to present a confusing, and often contradictory, picture. Most investigators agree, however, that the best available theoretical and numerical models are unable to explain observations of wave evolution over the whole range of wind and wave speeds. Ursell (1956) remarked that 'wind blowing over a water surface generates waves in the water by physical processes which cannot be regarded as known.' Whilst our knowledge has certainly advanced over the past forty years, as recently as 1990, Donelan & Hui observed that ' ... our knowledge of the wind input into the waves is still rather primitive. The theoretical ideas of the fifties have not been capable of explaining the observed growth rates and essentially no new ideas have followed.'

A principal motivation for continued study of wind–waves is the disparity between observed values of the rate of energy transfer from the air flow to the wave motions and the, considerably smaller, values obtained from analytical and numerical models. For example, Hasselmann & Bösenberg (1991) concluded that the best available models gave values of γ (the rate of energy transfer from wind to waves per unit time per radian) a factor of about two smaller than values they measured at sea. Figure 1(*a*) is reproduced from Plant (1984), who collated and plotted measurements of γ/f_W, against u_{*a}/c on logarithmic axes (here u_{*a} is the friction velocity in the air, c wave phase speed and f_W is the frequency of the wave). Despite considerable scatter, even on logarithmic axes, the data follow approximately a power law, at least for large values of u_{*a}/c. Hence Plant suggested that

$$\gamma/f_W = 2\pi\frac{\rho_a}{\rho_w}\beta(u_{*a}/c)^2 \tag{1.1}$$

(ρ_a and ρ_w are the densities of air and water) and Plant found emperically that $\beta = 32 \pm 16$. Whilst Plant's correlation has certainly been useful in guiding developments, the axes in figure 1(*a*) tend to exaggerate small values of c/u_{*a} (i.e. less than about 5), which are commonly measured in laboratory experiments. In the field c/u_{*a} has moderate to large values (which range from about 5 to 20 in Snyder *et al.*'s 1981 experiments) that are tightly bunched on Plant's correlation. Plant's correlation has become the benchmark test for theoretical and numerical models, but, since it masks the range of c/u_{*a} that is applicable to the ocean, we do not believe it to be sufficient validification of a theory or model: comparisons of other quantities such as vertical profiles of streamwise-velocity perturbation and shear stress (which have both been measured in laboratory experiments, e.g. Hsu, Hsu & Street 1981; Hsu & Hsu 1983) are also required.

We focus on the oceanic range of c/u_{*a} and figure 1(*b*) shows the data collected by Plant (1984) replotted with β against c/u_{*a} on linear axes. Figure 1(*b*) shows how data that follow a quadratic dependence on c/u_{*a} in figure 1(*a*), which therefore has β constant, are only a small fraction of the total range of c/u_{*a} values. Of

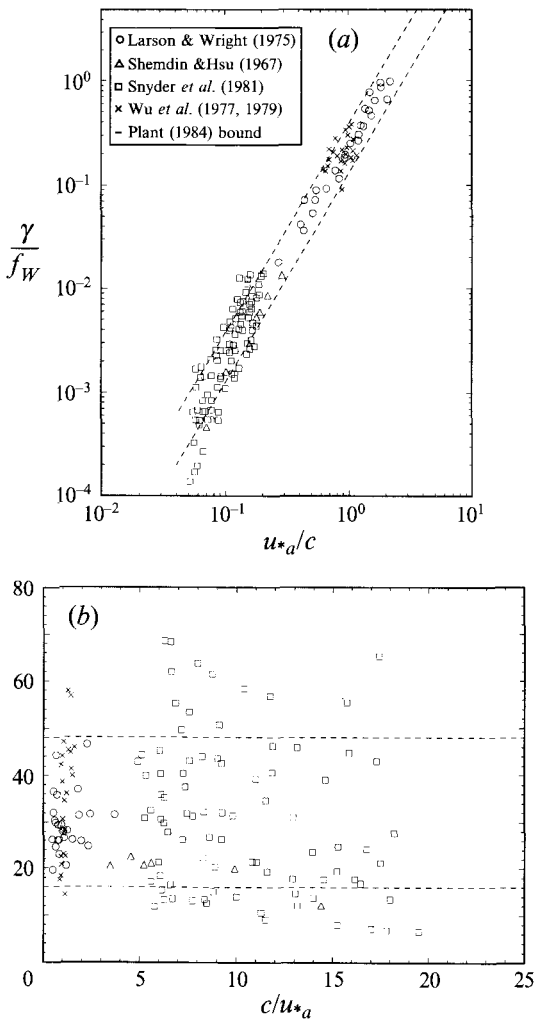

FIGURE 1. Data collected by Plant (1984) for growth rate of wave energy: (*a*) logarithmic axes; (*b*) linear axes.

course, the data in figure 1(*b*) show large scatter, but β does seem to decrease systematically as c/u_{*a} increases. Scatter in the data has been attributed by some experimental investigators to variation of parameters other than c/u_{*a} (Snyder *et al.* 1981); whereas other experimentalists (Hasselmann & Bösenberg 1991) have dismissed the importance of other parameters. We consider in detail which parameters can cause significant variations of β in Belcher, Harris & Street (1994, hereafter referred to as Part 3).

In an effort to address some of these deficiencies of present models, we study the processes that control energy and momentum exchange across the air–sea interface by developing theoretical and numerical models that are compared with data and other models. In this first part of our study, we focus on some theoretical aspects of the flow and develop an analytical model for the coupled turbulent air–water flow. Harris, Belcher & Street (1994, hereafter referred to as Part 2), describe a numerical model of the coupled air–water flow and systematically compare profiles of the velocity and

shear stress with the analytical model and experimental data. Finally, in Part 3, we examine the energy budget of wave motions by using results from the theoretical and numerical models. One of the overall goals of our studies is to compare results from our models and those of others with the data plotted in figure 1(*b*).

We address in detail the role played in the development of wind waves by the wind-driven drift current in the water. This current is generated by the shear stress exerted by the wind at the water surface. Laboratory measurements of this water-side boundary layer (e.g. Wu 1975; Cheung & Street 1988) show that it is fully turbulent even at low wind speeds. It is already known that theoretical values for the growth rate of short-wavelength capillary–gravity waves change significantly when the coupling between air and water motions is properly analysed (Valenzuela 1976; van Gastel, Janssen & Komen 1985). But for longer wavelengths the role of the sheared drift current is not well understood. Consequently, we analyse fully coupled models of air–water flow with a wavy interface. In this first part of the study the analytical model of air flow over an irrotational wave developed by Belcher & Hunt (1993) is extended to account for perturbations to the sheared drift current in the water. The numerical model described in Part 2 also accounts for motions in the water.

Following most previous investigators, we imagine a base flow that consists of an air–water flow with a flat interface. In §2, scaling arguments are developed to justify the form of base flow that we use. Superimposed onto the base flow are two-dimensional waves of low slope that travel parallel to the wind. The linear changes to the unperturbed state induced by the wavy interface are then calculated (as described in §3). Linear changes are considered so that the problem is made tractable; moreover, careful interpretation of a linear analysis can give insight into the processes that persist in the air and water flows when the waves have larger slope. For example, Belcher & Hunt (1993) found that, when $u_*/(U_B(\lambda) - c) \ll 1$, a non-separated sheltering mechanism provides the largest contribution to the asymmetric surface pressure (and hence wind-input of energy to waves). This mechanism is clearly robust in the sense that it persists at large amplitudes. Nevertheless, we recognize that there are further nonlinear processes, associated with the deforming interface, that influence wind–wave interactions. For example, inviscid wave–wave interactions (Phillips 1960; Hasselmann 1962) and wave breaking (e.g. Banner & Peregrine 1993) are both nonlinear phenomena and so are neglected here. We assume that, for small-amplitude waves, energy transfer from wind to waves is unaffected by these nonlinear effects; their role in the evolution of wind-sea is modelled in the evolution equation for the wave-energy spectrum by transfer terms that are simply added to the wind input term (see e.g. the WAMDI Group 1988).

A critical question in modelling wind–wave interactions is the choice of turbulence model used to describe Reynolds stress (Davis 1972). In previous studies these models range from assuming the Reynolds stress has no effect on the flow perturbations (e.g. Miles 1957); using the simple mixing-length model throughout the flow (e.g. Gent & Taylor 1976); and using a two-equation turbulence model (e.g. Al-Zanaidi & Hui 1984, who used a kinetic energy–vorticity formulation). Only a few of the previous studies have reasoned their choice of turbulence model with physical argument: Townsend's (1980) study was based on a systematic extension of Townsend (1972); Belcher & Hunt (1993) used a theoretical scaling developed by Belcher, Newley & Hunt (1993) to motivate their choice of model. The turbulence model used by Belcher & Hunt (1993) is appropriate for air flow over slowly moving waves, and, in §4, we generalize their arguments to investigate the response of the turbulence to waves of arbitrary speed. We then propose a way of classifying wind–wave flow into different

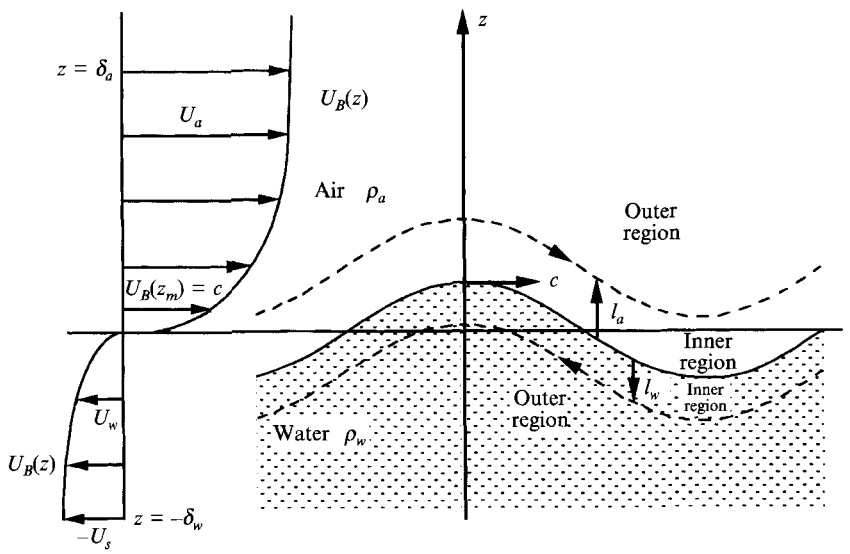

FIGURE 2. Definition sketch of the flow geometry in a frame of reference that moves at the speed of the unperturbed drift current at the water surface.

parameter regimes where different types of turbulence model are needed to model the air flow successfully. This classification is central to our work and determines the choice of turbulence models used in the analytical and numerical studies. Similar arguments are also used to develop a turbulence model for the water-side boundary layer. The sensitive role of the turbulence model is exemplified by recent asymptotic studies of air flow over prescribed waves (Jacobs 1987; van Duin & Janssen 1992; Belcher & Hunt 1993) that use turbulence models of apparently only slightly different form, but obtain results that are qualitatively different. In §7 we compare these theories and show how and why the different turbulence models give qualitatively different results for key quantities, such as the asymmetric pressure (which controls energy transfer to the wave motion).

2. Base flow profiles and timescales

Air flows in the x-direction as a turbulent boundary layer over a flat water surface at $z = 0$. The wind stress exerted at the water surface drags a sheared drift current in the water, which has speed U_s at the surface and decays to zero far below the interface. This is defined here to be the *base* or *unperturbed* flow. We perform calculations in a frame of reference where there is no flow at the interface; the sheared drift current is then zero at the interface and asymptotes to $-U_s$ far below the interface. Base flow profiles and the flow geometry are sketched in figure 2.

In the presence of interfacial waves, a distinction has to be made between the base flow and the *wave-averaged* flow; the latter is defined here to be the time-average of experimental measurements (or numerical simulations) of air flow over waves and water flow under waves. The wave-averaged flow is composed of the base flow plus the average over many wavelengths of wave-induced perturbations, which can be significant despite being of second order in wave slope. In an experiment, waves are always present so that direct measurement of the base flow is difficult and care must be exercised in establishing properties of the base flow from profiles of wave-averaged

experimental measurements. As discussed in Part 2, this difficulty is particularly acute when deriving the unperturbed friction velocity from experimental data (usually the wave-averaged friction velocity is cited). Finally, in this study, the term *mean* flow is used to describe the ensemble-averaged flow (so that turbulent fluctuations have been averaged out).

This approach of modelling the wind–wave flow as a base flow plus perturbations differs from recent studies of the development of a wind-induced drift current in the presence of waves (Jenkins 1987; Weber & Melsom 1993). The cited investigations seem to assume without justification that the wind exterts no unperturbed stress at the sea surface: the stress at the interface comes entirely from wave-averaged perturbations to the air flow. In §2.2 we present timescale analyses which suggest that this latter approach is not self-consistent.

2.1. *Base flow in the air*

In the unperturbed state, the air flows as a neutrally stable atmospheric boundary layer, which has a typical depth, δ_a, of about 1 km (where its growth is limited by Coriolis effects). The Reynolds number (based on geostrophic wind speed and boundary-layer thickness) is very large and the unperturbed-velocity profile, U_B, is logarithmic from near the surface (where the flow may be rough, transitional or smooth depending on the sea state) up to about one fifth of the boundary-layer depth (Townsend 1976), i.e. up to about 200 m. In the analytical model, the unperturbed-velocity profile is assumed logarithmic through all depths of interest (which are defined in §5) and so the shear stress is constant, hence

$$U_B(z) = (u_{*a}/\kappa)\ln(z/z_0), \qquad \tau_B(z) = \rho_a u_{*a}^2, \tag{2.1}$$

where ρ_a is the density of air, u_{*a} is the unperturbed friction velocity in the air flow, $\kappa = 0.4$ is the von Kármán constant and z_0 is the roughness length of the surface (or the equivalent roughness of a smooth surface). In the theoretical study, rough interfaces only are considered (although the theory can be extended to smooth interfaces); in Part 2, where the numerical model is described, different interfacial conditions are treated more thoroughly.

2.2. *Base flow in the water*

When wind blows over water the shear stress exerted by the wind at the surface drives a current in the water. Measurements, e.g. Cheung & Street (1988), show that, even at low wind speeds, the sheared current in the water is turbulent. We therefore model the sheared current in the water as a zero-pressure-gradient turbulent boundary layer. In the inner region (defined in §4) of the water flow the velocity profile is assumed logarithmic and the shear stress constant, so that

$$U_B(z) = -(u_{*w}/\kappa)\ln(-z/z_0), \qquad \tau_B(z) = \rho_w u_{*w}^2, \tag{2.2}$$

where u_{*w} is the friction velocity in the water flow, ρ_w is the density of water and z_0 is the roughness length of the surface, which for simplicity is assumed to be the same as in the air flow (Kondo 1976). Outside the inner region, U_B is assumed monotonic decreasing, but for the linear theory it does not have to be specified exactly. Continuity of shear stress at the interface implies that

$$\rho_a u_{*a}^2 = \rho_w u_{*w}^2. \tag{2.3}$$

Our model for the base flow in the water requires justification because, in a fetch-limited flow, or when the wind suddenly starts blowing, the sheared current grows in

depth. It is therefore appropriate to examine the timescale on which the depth, δ_w, of the wind-driven boundary layer grows and compare it with the timescale on which waves grow. To do this, it is assumed that waves do not affect boundary-layer growth. Since waves promote mixing (Komori, Nagaosa & Murakami 1993) and therefore accelerate growth of the wind-driven boundary layer, the following estimates of δ_w are likely to be lower bounds. Ultimately, growth of the boundary layer is limited by other physical processes. For example, stable stratification could control δ_w, or, in a neutrally stratified flow, growth of the drift-current boundary layer can be limited by Coriolis force, which imposes a depth scale of $O(u_{*w}/f_C) \approx 30\,\mathrm{m}$ (here f_C is the Coriolis parameter).

The sheared current in the water is considered to be a neutrally stratified turbulent boundary layer, whose depth, δ_w, at time t may be estimated from

$$\delta_w \sim (\nu_t t)^{\frac{1}{2}}, \tag{2.4}$$

where ν_t is the eddy viscosity. In the outer part of the boundary layer, which controls its growth into the ambient fluid below, ν_t scales on the friction velocity, u_{*w}, and the boundary-layer depth so that (2.4) implies

$$\delta_w \sim u_{*w} t. \tag{2.5}$$

Anticipating the results of §6.3, wave growth is exponential, $a(t) = a(0)\exp(t/T_G)$, with e-folding time T_G that scales as

$$T_G \sim \frac{\rho_w}{\rho_a}\frac{u_{*a}^2}{c^2} T_W, \tag{2.6}$$

where T_W is the period and c is the phase speed of the wave.

The depth scale, l_w, of the inner region (defined in §4.2) is the depth scale of a thin layer in the water near the interface where turbulent stresses significantly affect flow perturbations and it scales as

$$l_w \sim \frac{u_{*w}}{U_w + c}\lambda \sim u_{*w} T_W, \tag{2.7}$$

where λ is the wavelength and U_w is a velocity scale for the base flow in the water (it is defined precisely in §5). The second relation in (2.7) is obtained because $U_w \ll c$ for most wind–wave systems (see §6). If $l_w \ll \delta_w$ then interactive perturbations are induced in the drift current and it can affect wave growth. From (2.5), the drift-current boundary layer grows to depth l_w after a time l_w/u_{*w} and in this time the wave amplitude, $a(t)$, grows to

$$a(t) \sim a(0)\exp\left(\frac{\rho_a}{\rho_w}\frac{c^2}{u_{*a}^2}\right). \tag{2.8}$$

For c/u_{*a} in the range 1–30 (which implies wavelengths in the range 0.1–100 m if $u_{*a} = 0.5\,\mathrm{m\,s^{-1}}$) the wave amplitude grows by a factor of $\mathrm{e}^{1/1000}$–e^{1}. It is interesting that longer waves (with larger c/u_{*a}) grow on a timescale that is comparable with the timescale for growth of the drift current. The analysis to be presented in §5 is valid when $l_w \ll \delta_w$; a suitable value for practical purposes is $l_w \lesssim \delta_w/5$. Our scaling analysis indicates that, for most waves, this condition is satisfied before the waves have grown significantly.

But does the unsteadiness of δ_w (and hence the unsteadiness of velocity profile in the water) affect perturbations to the flow? To answer this question, we examine how

much the depth of the drift current increases compared with a wavelength in one wave period, i.e. consider the ratio

$$\frac{\mathrm{d}\delta_w/\mathrm{d}t}{\lambda/T_W} \sim u_{*w}/c = \left(\frac{\rho_a}{\rho_w}\right)^{\frac{1}{2}} u_{*a}/c \ll 1. \tag{2.9}$$

The unperturbed flow in the drift current is therefore modelled as being steady.

Most previous studies of wind–wave generation have assumed that the flow in the water is inviscid and irrotational, but this is not consistent with laboratory studies even for short times after wind starts blowing (e.g. Wu 1975; Cheung & Street 1988). The waves have a period, T_W, that is much smaller than the timescale, T_C, for the drift current to grow significantly (compared with λ), $T_C \sim T_W(\rho_w/\rho_a)^{\frac{1}{2}}$, which is in turn much smaller than the timescale for wave growth, $T_G \sim T_W(\rho_w/\rho_a)$. It therefore seems justified and worthwhile to model the sheared layer in the water as a fully developed turbulent boundary layer that is steady in time.

3. Formulation of the perturbed-flow model

Now consider flow over and under a travelling wave, $z = \eta(x - ct)$. Here, the wave phase speed, c, is measured relative to the coordinate system that moves to the right with speed U_s, so that the base flow is zero at the interface in this frame of reference. Flow with the wave is expressed as the base flow (defined in §2) plus a perturbation, e.g. horizontal velocity $\mathscr{U} = U_B + \Delta u$ and the Reynolds stress tensor $\mathscr{T}_{ij} = T_{ij} + \Delta\tau_{ij}$. Pressure is referred to hydrostatic pressure, which is defined from the instantaneous water surface, so that, if $\mathscr{P}$ is the total pressure, $\mathscr{P} = P_B + \Delta p + \rho_\alpha g'(\eta - z)$. Pressure at the interface is then $P_B + \Delta p$. The wave slope, ak, is assumed small so that equations governing the perturbations can be linearized about the undisturbed state,

$$\frac{\partial \Delta u}{\partial t} + U_B\frac{\partial \Delta u}{\partial x} + \Delta w\frac{\mathrm{d}U_B}{\mathrm{d}z} = -\frac{1}{\rho_\alpha}\frac{\partial \Delta p}{\partial x} - g'\frac{\partial \eta}{\partial x}\mathrm{H}(\eta - z) + \frac{\partial \Delta\tau}{\partial z} + \frac{\partial \Delta\tau_{xx}}{\partial x}, \tag{3.1}$$

$$\frac{\partial \Delta w}{\partial t} + U_B\frac{\partial \Delta w}{\partial x} = -\frac{1}{\rho_\alpha}\frac{\partial \Delta p}{\partial z} + \frac{\partial \Delta\tau}{\partial x} + \frac{\partial \Delta\tau_{zz}}{\partial z}, \tag{3.2}$$

$$\frac{\partial \Delta u}{\partial x} + \frac{\partial \Delta w}{\partial z} = 0, \tag{3.3}$$

where subscript α refers to either in the air or water, H is the Heaviside step function and $g' = g(\rho_w - \rho_a)/\rho_w$ is reduced gravity. In the above equations, the roughness Reynolds number, $u_{*a}z_0/\nu$, is assumed to be sufficiently large that the flow is aerodynamically rough and the viscous stresses can be neglected throughout the flow. Far above and below the interface the perturbations decay, i.e.

$$\left.\begin{aligned} \Delta u \to 0,\quad \Delta w \to 0,\quad \Delta\tau \to 0,\quad \Delta p \to 0, \qquad & \text{as } z \to \infty, \\ \Delta u \to 0,\quad \Delta w \to 0,\quad \Delta\tau \to 0,\quad \Delta p \to -\rho_w g'\eta, \qquad & \text{as } z \to -\infty. \end{aligned}\right\} \tag{3.4}$$

The lower boundary condition on Δp ensures that the total pressure is just the hydrodynamic head. At the interface the velocity is continuous and therefore the vertical velocity equals the vertical speed of the interface

$$\Delta u_a(0) = \Delta u_w(0), \qquad \Delta w_a(0) = \Delta w_w(0) = \frac{\mathrm{D}\eta}{\mathrm{D}t}. \tag{3.5}$$

A dynamical boundary condition is also required at the interface. Since surface tension may be neglected for long enough waves, the normal stress is continuous.

The boundary condition on tangential stress depends on conditions at the interface. Here we suppose that the small ripples at the surface are in a local equlibrium with the wind so that shear stress is continuous across the interface. To leading order in ak, this implies the following coupling conditions on the pressure and shear-stress perturbations:

$$-\Delta p_a(0) + \Delta\tau_{zza}(0) = -\Delta p_w(0) + \Delta\tau_{zzw}(0), \qquad \Delta\tau_a(0) = \Delta\tau_w(0). \tag{3.6}$$

3.1. *Transformation to wave-following coordinates*

A wave-following coordinate system (X, Z, T) is defined, following Hsu *et al.* (1981) and others, by

$$t = T, \quad x = X, \quad z = Z + f(Z)\eta(X, T), \tag{3.7}$$

where, by construction, the interface, $z = \eta$, is defined by $Z = 0$, i.e. $f(0) = 1$. A similar, but orthogonal, transformation was used by Benjamin (1959) and Belcher & Hunt (1993). The function f is defined so that the lines of constant Z are wave-induced streamlines produced if the flow were irrotational, so that for a sinusoidal wave $\eta = \mathrm{Re}\{a\,\mathrm{e}^{\mathrm{i}k(x-ct)}\}$ and flow that is unconfined in the vertical

$$f = \begin{cases} \mathrm{e}^{-kZ}, & Z \leqslant 0, \\ \mathrm{e}^{kZ}, & Z \geqslant 0. \end{cases} \tag{3.8}$$

In the wave-following coordinates the vertical-velocity perturbation is separated into two parts,

$$\Delta w = -(c - U_B) f \partial\eta/\partial X + \Delta w_d, \tag{3.9}$$

where the first part is the vertical velocity that would be induced in inviscid irrotational flow over the wave. Other pertubation quantities are defined as equal to those in the Cartesian coordinates, e.g. $\Delta u(x, z) = \Delta u_d(X, Z)$.

On using the chain rule and definition of Δw_d, the equations governing linear perturbations in the wave-following coordinates become

$$\frac{\partial \Delta u_d}{\partial T} + U_B \frac{\partial \Delta u_d}{\partial X} + \Delta w_d \frac{\mathrm{d}U_B}{\mathrm{d}Z} = -\frac{1}{\rho_\alpha}\frac{\partial \Delta p_d}{\partial X} - g'\frac{\partial \eta}{\partial X}\mathrm{H}(-Z) + \frac{\partial \Delta\tau_d}{\partial Z} + \frac{\partial \Delta\tau_{XX}}{\partial X}, \tag{3.10}$$

$$\frac{\partial \Delta w_d}{\partial T} + U_B \frac{\partial \Delta w_d}{\partial X} + (c - U_B)^2 f \frac{\partial^2 \eta}{\partial X^2} = -\frac{1}{\rho_\alpha}\frac{\partial \Delta p_d}{\partial Z} + \frac{\partial \Delta\tau_d}{\partial X} + \frac{\partial \Delta\tau_{ZZ}}{\partial Z}, \tag{3.11}$$

$$\frac{\partial \Delta u_d}{\partial X} + \frac{\partial \Delta w_d}{\partial Z} = (c - U_B) f' \frac{\partial \eta}{\partial X}. \tag{3.12}$$

Equations (3.10) and (3.11) actually have two additional terms that arise from the coordinate transformation. But these terms are negligible because they are products of the vertical-coordinate stretching, f, and gradients of unperturbed Reynolds stress, $\partial T_{ij}/\partial X_j$: namely,

$$f(\partial\eta/\partial X)(\mathrm{d}T_{XX}/\mathrm{d}Z), \quad f'\mathrm{d}T_{XZ}/\mathrm{d}Z \tag{3.13}$$

on the right hand side of (3.10) and

$$-f(\partial\eta/\partial X)(\mathrm{d}T_{XZ}/\mathrm{d}Z), \quad -f'\mathrm{d}T_{ZZ}/\mathrm{d}Z \tag{3.14}$$

on the right hand side of (3.11). These terms are all smaller than the retained terms

because the unperturbed flow is in the logarithmic part of the boundary layer where the unperturbed stress, T_{ij}, is approximately constant (Townsend 1976).

Boundary conditions far from the interface are unchanged by the coordinate transformation, but the kinematical condition at the interface is modified by the definition of Δw_d and becomes

$$\Delta w_d = 0 \quad \text{at } Z = 0. \tag{3.15}$$

In the following the wave-following coordinate system is used throughout but the subscript d is dropped.

Velocity perturbations scale on $U_{0\alpha}$ (where α denotes either air or water), which is a value of the unperturbed velocity relative to the wave speed and is defined more precisely in §5.3. The undulating shape of the wave induces a pressure perturbation that scales as $\rho_\alpha U_{0\alpha}^2$, where ρ_α is the density of air or water. Finally, Reynolds-stress perturbations scale on $\rho_\alpha u_{*\alpha}^2$, the base-flow shear stress in the air or water. These scalings are next used to examine how turbulence in the unperturbed flow is affected by the wave, which leads to suggestions for turbulence models that can be used for the perturbed flow.

4. Turbulence models for the perturbed flow

Belcher *et al.* (1993) developed timescale arguments to examine how boundary-layer turbulence is affected by a slowly moving wave. We now extend these arguments to consider waves of arbitrary speed and to consider turbulence in the water flow. Accordingly, a distinction is made between the types of turbulence model that are appropriate for modelling the base flow and the perturbations to that base flow. As described in §2, unperturbed profiles in the air and water are considered to be zero-pressure-gradient turbulent boundary layers, so that the turbulence is in a local equilibrium and a simple eddy-viscosity model is adequate. The Reynolds stress in the perturbed flow is, as we shall demonstrate, governed by more complex dynamics and a simple eddy viscosity is appropriate over only a small portion of the flow domain.

4.1. *Turbulence in the air flow*

Timescales of some of the dynamical processes that affect the turbulence in the air are first investigated. In general these timescales must be related to properties of the nonlinear perturbed flow over a wave; for small changes to the flow, however, the timescales can be related to properties of the unperturbed boundary layer, with relative errors of $O(ak)$.

Following Belcher *et al.* (1993), define a timescale, T_D, for a turbulent eddy in the air to be advected and distorted by the flow as it passes over a wave that moves with speed c (it is the speed of a fluid element relative to the wave that is relevant),

$$T_D = \frac{k^{-1}}{|U_B(Z) - c|}. \tag{4.1}$$

A second timescale is T_L, a Lagrangian timescale for eddies to interact with one another and become decorrelated. In the logarithmic part of a turbulent boundary layer

$$T_L = \kappa Z / u_{*a}. \tag{4.2}$$

In a general turbulent flow additional processes affect the turbulence over different timescales, for example mean shear has a timescale $(\partial U_B/\partial Z)^{-1}$. In the logarithmic

portion of a turbulent boundary, however, these other timescales are proportional to T_L, because there are no velocity and length scales other than u_{*a} and Z in the logarithmic layer (Tennekes & Lumley 1972, p. 147).

Hence there are two timescales that control small perturbations to the turbulence and they are comparable, $T_D \sim T_L$, at a height l_a, where, for the logarithmic mean-velocity profile, $kl_a\{\ln(l_a/z_0) - \kappa c/u_{*a}\} \sim 1$. It is convenient in the analytical model described in §5 if the constant is chosen such that

$$kl_a\{\ln(l_a/z_0) - \kappa c/u_{*a}\} = 2\kappa^2. \tag{4.3}$$

In an inner region, where $Z \ll l_a$, eddies decorrelate and turn over many times before being advected over a wavelength, i.e. $T_L \ll T_D$. The turbulence is therefore in a local equilibrium and an eddy viscosity can be used to relate the Reynolds stress to the local mean-velocity gradient. Conversely, in the outer region, where $Z \gg l_a$ and $T_L \gg T_D$, eddies are advected over the wave before they have time to decorrelate or interact with one another. Hence the turbulence in the outer region is controlled by rapid distortion. If an eddy-viscosity model is erroneously used in the outer region then values computed for the asymmetric pressure and hence the growth rate of the wave are qualitatively in error (see Belcher & Hunt 1993 and §7). When $Z \sim l_a$ all terms in the equation governing perturbed turbulent kinetic energy are significant. Further details can be found in Belcher *et al.* (1993).

4.2. *Turbulence in the water flow*

Changes to the turbulence in the water-side boundary layer are examined using similar methods. There are two changes to the analysis of §4.1: the friction velocity is different and equal to $u_{*w} = (\rho_a/\rho_w)^{\frac{1}{2}} u_{*a}$ and the distortion timescale changes to

$$T_D = \frac{k^{-1}}{|U_B(Z) + c|}, \tag{4.4}$$

because, in the frame of reference that moves with the wave, the water flow is from right to left and of magnitude $|U_B(Z) + c|$ (see figure 2). The depth scale of the inner region in the water, l_w, is then defined implicity by

$$kl_w \left\{ \ln(l_w/z_0) + \frac{\kappa c}{u_{*a}} \left(\frac{\rho_w}{\rho_a}\right)^{\frac{1}{2}} \right\} = 2\kappa^2. \tag{4.5}$$

Flow in the water is divided into inner and outer regions like in the air flow. As c/u_{*a} increases, l_w rapidly decreases because $\rho_w/\rho_a \gg 1$, so that, for all but very small values of c/u_{*a},

$$kl_w \sim 2\kappa(\rho_a/\rho_w)^{\frac{1}{2}}(u_{*a}/c) \ll 1. \tag{4.6}$$

The region of flow subjected to rapid distortion is therefore a large fraction of the flow over the whole range of c/u_{*a} (> 0).

4.3. *Classification of flow regimes and turbulence models for the air flow*

Figure 3 shows vertical profiles of T_D and T_L in the air flow for a range of values of c/u_{*a} and with $kz_0 = 10^{-5}$ (similar behaviour is observed at other values of kz_0). This graph confirms the suggestion that $T_L \ll T_D$ near the interface. Notice how there is a logarithmic singularity with $T_D \to \infty$ at the matched height, z_m, where $U_B(z_m) = c$. The depth kl_a is proportional to the height where the curves T_D and T_L cross, and figure 3 shows that as c/u_{*a} increases, l_a and z_m move further from the interface. We

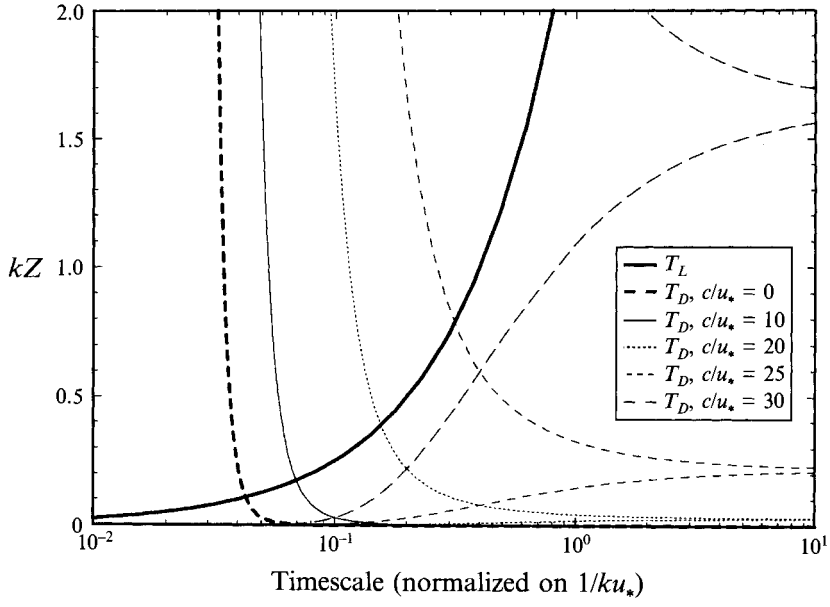

FIGURE 3. Advection and eddy-turnover timescales in the air flow ($kz_0 = 10^{-5}$); l_a is proportional to the height where $T_D = T_L$.

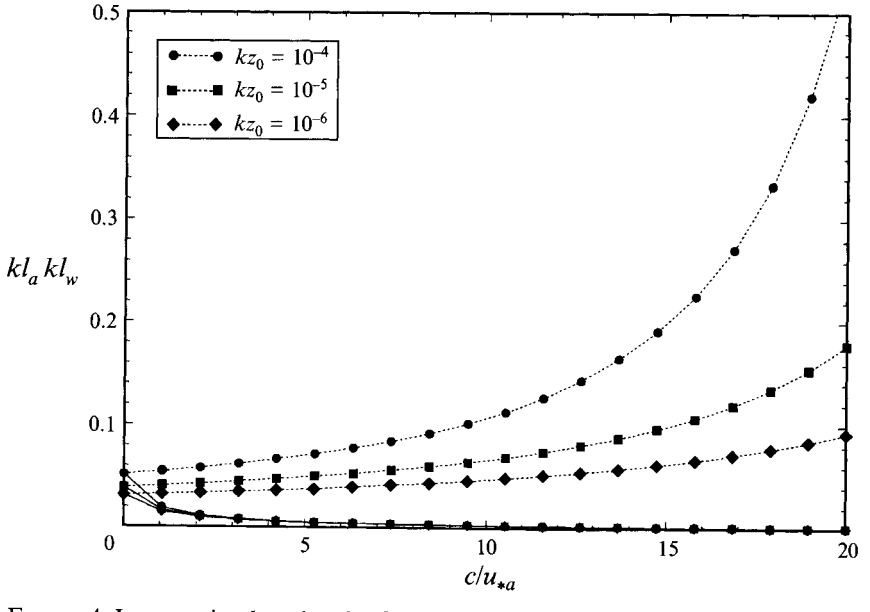

FIGURE 4. Inner-region lengthscales for air and water flows: dotted lines, kl_a; solid lines, kl_w.

propose that different regimes of wind–wave flow can be identified at different values of $kl_a/(2\kappa^2)$, the relative depth of the inner region in the air flow. Variation of kl_a and kl_w with c/u_{*a} is shown in figure 4.

To capture completely the Reynolds-stress changes throughout the flow over the whole range of wind and wave speeds, it is necessary to use a turbulence model that

contains both the rapid-distortion mechanism and local-equilibrium effects. Second-order-closure models (e.g. Zeman 1981) that have transport equations for each stress component satisfy these criteria, but they are computationally expensive to solve and are not without their own problems (particularly in the near-wall region, see Belcher *et al.* 1993; Durbin 1993). Townsend (1980) constructed a simplified second-order-closure model precisely to be a local-equilibrium model near an interface, and to relax (through an advection–diffusion equation) to rapid distortion far from the interface. In Part 2 we follow a different, and new, approach. The $k-\varepsilon$ model is modified so that the eddy viscosity decays to zero outside the inner region. This procedure gives a model that is valid across the whole range of wind and wave speeds and that is computationally cheap. Next we examine the limiting cases of *fast* and *slow* waves, when simpler turbulence models can be used.

4.3.1. *Slow waves*

We use the term slow waves to denote wind–wave systems with $kl_a/(2\kappa^2) \ll 1$, so that the scale height of the inner region is much smaller than a wavelength. A working approximation is that $kl_a/(2\kappa^2) \lesssim \frac{1}{2}$. This is the parameter regime studied by Belcher & Hunt (1993). In §5 their analysis is extended to include the turbulent motions in the water.

Following Belcher *et al.* (1993), where details can be found, we use a *truncated mixing-length model* for slow waves. This is a simple approach that is consistent with the limiting behaviours in the inner and outer regions. Throughout the inner region, the turbulence is modelled as if in perfect local equilibrium. And so the Reynolds shear stress is approximated with the mixing-length model and normal-stress perturbations are proportional to the shear-stress perturbation

$$\Delta\tau = 2\kappa u_{*a} Z\,\partial\Delta u/\partial Z, \qquad \Delta\tau_{XX} = -c_1\Delta\tau, \qquad \Delta\tau_{ZZ} = -c_2\Delta\tau, \tag{4.7}$$

where $c_1 = 6.3$ and $c_2 = 4.5$ (Townsend 1976). The leading-order formula for the wave growth is dependent only on the model for the shear stress, and so is independent of c_1 and c_2 (see §5.5). In the outer region, Reynolds-stress perturbations are modelled using rapid-distortion theory (RDT), which shows that, to the linear approximation, $\Delta\tau_{ij} = O(ak\,u_{*a}^2)$. This implies that, in the momentum equations (3.10) and (3.11), the Reynolds-stress gradients are much smaller than the inertial gradients,

$$\frac{\partial\Delta\tau_{XX}/\partial X}{U_B\partial\Delta u/\partial X} = O\left(\frac{aku_{*a}^2/\lambda}{akU_{0a}^2/\lambda}\right) = O\left(\frac{u_{*a}^2}{U_{0a}^2}\right) \ll 1. \tag{4.8}$$

Leading-order perturbations in the outer region are therefore calculated by setting gradients of Reynolds stress to zero, so that the momentum equations are inviscid. Hence, essential changes to the flow can be calculated without performing detailed RDT calculations. Hence the mixing-length model is truncated above the inner region.

4.3.2. *Fast waves*

For moderate to large values of c/u_{*a}, $kl_a/(2\kappa^2)$ is approximately equal to or greater than one. Waves with $kl_a/(2\kappa^2) \gtrsim 1$, we call fast. In this regime figure 3 shows that T_L is smaller than T_D at all heights below l_a; hence, an eddy-viscosity model is valid up to $Z \sim l_a$. Furthermore, field measurements of Snyder *et al.* (1981) show that the pressure perturbation decays away from the interface as e^{-kZ} (theory for slow waves is in agreement, Belcher & Hunt 1993); hence, for fast waves, perturbations to the flow induced by the wave are exponentially small in the region of flow affected by

rapid distortion (when $Z \gg l_a$). For these waves, an eddy-viscosity model may be used throughout the flow: there is no significant outer region.

When waves travel extremely quickly, there can be a layer between the matched height and the interface where T_D is less than T_L. There is then a region of rapid distortion between two layers of equilibrium dynamics (one next to the interface and the other around the matched height). This region appears when $U_B(l_a) - c$ in (4.1) is negative; equation (4.3) then has two new solutions if

$$c/u_{*a} \geqslant \{\ln(2\kappa^2/kz_0) + 1\}/\kappa, \tag{4.9}$$

which implies that $c/u_{*a} \geqslant 28$ when $kz_0 = 10^{-5}$. These are very fast waves and are not considered further in this study.

4.4. *Turbulence model for the water flow*

Variation of the inner-region scale height, kl_w, with c/u_{*a} is plotted in figure 4. For the waves travelling with the wind considered here, kl_w decreases rapidly with c/u_{*a}, because the square root of the density ratio factors into the definition of l_w (4.5). Hence, in the water, over the whole range of wind and wave speeds, $kl_w/(2\kappa^2)$ is much less than one (provided kz_0 is small, as it is in practical situations). The outer region, where rapid distortion controls changes to the turbulence, therefore plays a decisive role in the water flow. We use the truncated mixing-length model in the water flow through all parameter regimes (provided $c/u_{*a} > 0$). In §7 we show that, if the mixing-length model is used in the outer region of the water flow, the results are completely unphysical.

5. Analysis of slow waves

The perturbation analysis is performed in terms of normal modes, so that the interface has a two-dimensional wave with sinusoidal variation in time and space,

$$\eta = a\mathrm{Re}\{e^{ik(x-ct)}\}, \tag{5.1}$$

where Re denotes real part. Linear perturbations forced by the wave are analysed as follows. In §5.1 and §5.2 we transform the equations that govern the perturbations (3.10)–(3.12) into a generic form, namely the equations that govern flow over a hill. To begin, these equations are considered with the boundary condition that streamwise velocity is zero at the interface. These equations and boundary conditions have been solved by Hunt, Leibovich & Richards (1988) and extended to higher order by Belcher *et al.* (1993). Their method of solution is outlined in §5.3. In subsequent sections, we consider the remaining interfacial boundary conditions. The perturbation to the streamwise velocity at the surface is allowed to be non-zero in §5.4, which induces further perturbations to the flow and makes it possible to match shear stress across the interface. Finally, in §5.5 pressure is matched across the interface to determine the wave speed and growth rate.

5.1. *Flow in the air*

Linear perturbations to the air flow vary in x and t in the same way as η, hence scaled dimensionless variables are formed:

$$\left.\begin{aligned} \Delta u_a &= \mathrm{Re}\{U_{0a}\hat{u}(\hat{Z})k\eta\}, & \Delta w_a &= \mathrm{Re}\{U_{0a}\hat{w}(\hat{Z})k\eta\}, \\ \Delta p_a &= \mathrm{Re}\{\rho_a U_{0a}^2\hat{\sigma}(\hat{Z})k\eta\}, & \Delta\tau_a &= \mathrm{Re}\{\rho_a u_{*a}^2\hat{\tau}(\hat{Z})k\eta\}, \end{aligned}\right\} \tag{5.2}$$

where $\hat{Z} = kZ$ and U_{0a} is an unperturbed-velocity scale in the air (defined in §5.3.1) which is also used to make the base-flow profile non-dimensional, so that $\hat{U}_B = U_B/U_{0a}$. The characteristic slope of the wave, ak, is assumed small, so that $|k\eta| \ll 1$. The unsteady term in each momentum equation (e.g. $-\mathrm{i}kc\hat{u}$ in the x-momentum equation) can be absorbed into the definition of unperturbed velocity if

$$\hat{U} = \hat{U}_B - \frac{c}{U_{0a}} \equiv \frac{\epsilon_a}{\kappa} \ln(\hat{Z}/z_{ma}). \tag{5.3}$$

Here $z_{ma} = kz_0 \exp(\kappa c/u_{*a})$ is the matched height, where the unperturbed wind speed equals the wave phase speed. These expressions are substituted into (3.10)–(3.12), which become

$$\hat{U}\,\mathrm{i}\hat{u} + \hat{w}\frac{\mathrm{d}\hat{U}}{\mathrm{d}\hat{Z}} = -\mathrm{i}\hat{\sigma} + \epsilon_a^2\left(\frac{\mathrm{d}\hat{\tau}}{\mathrm{d}\hat{Z}} + \mathrm{i}\hat{\tau}_{XX}\right), \tag{5.4}$$

$$\hat{U}\,\mathrm{i}\hat{w} = -\frac{\mathrm{d}\hat{\sigma}}{\mathrm{d}\hat{Z}} + \epsilon_a^2\left(\mathrm{i}\hat{\tau} + \frac{\mathrm{d}\hat{\tau}_{ZZ}}{\mathrm{d}\hat{Z}}\right) + \hat{U}^2 f, \tag{5.5}$$

$$\mathrm{i}\hat{u} + \frac{\mathrm{d}\hat{w}}{\mathrm{d}\hat{Z}} = -\hat{U}\,\mathrm{i}f', \tag{5.6}$$

where $\epsilon_a = u_{*a}/U_{0a}$ is a second small parameter (after the wave slope), which is typically 0.03–0.07 in the atmosphere. The following boundary conditions are applied:

$$\hat{u} = \hat{w} = 0 \quad \text{on } \hat{Z} = 0, \qquad \hat{u}, \hat{w}, \hat{\sigma}, \hat{\tau} \to 0 \quad \text{as } \hat{Z} \to \infty. \tag{5.7}$$

Hence to begin, set streamwise velocity at the interface to zero, i.e. $\Delta u(0) = 0$. Perturbations computed with this boundary condition are denoted with superscript (U). In §5.4, when the coupling condition on tangential stress is satisfied, $\Delta u(0)$ is allowed to be non-zero and further perturbations are induced in the flow. These perturbations can be analysed by considering flow over a flat surface that has a varying surface velocity. The two partial solutions can be added together because they are governed by linear equations (see also §5.4 and Belcher & Hunt 1993).

5.2. *Flow in the water*

In the water, the x-momentum equation (3.10) contains an extra term due to buoyancy, namely $g'\partial\eta/\partial X$, which is a variation in hydrostatic head due to the undulating level of the interface. It does not affect the dynamics of the water-flow perturbations; but is important when pressure is matched at the interface. Hence, pressure in the water is written as

$$\Delta p_w = \Delta\sigma(\hat{Z}) - \rho_w g'\eta. \tag{5.8}$$

Equations and boundary conditions governing the water-flow perturbations may be transformed into the same equations as those that govern air-flow perturbations. To do this the spatial coordinates are reflected, $\hat{X} = -kX$ and $\hat{Z} = -kZ$, thus mapping the domain of the water into the domain of the air. The wave travels against the unperturbed water flow and so $\hat{c} = -c$. When the air flow is at a wave crest, the water is at a trough of its motion, hence set $\hat{\eta} = -\eta(\hat{X}, \hat{c})$. In the water, the unperturbed velocity is from right to left, hence it is also reflected, $\hat{U}_B = -U_B/U_{0w} = (\epsilon_w/\kappa)\ln(\hat{Z}/z_0)$, where $\epsilon_w = u_{*w}/U_{0w}$ and U_{0w} is the velocity scale in the water (defined in §5.3.1). Furthermore, the unsteady terms in the momentum

equations can be absorbed into advection if

$$\hat{U} = c/U_{0w} - \hat{U}_B = c/U_{0w} + \frac{\epsilon_w}{\kappa}\ln(\hat{Z}/z_0) \equiv \frac{\epsilon_w}{\kappa}\ln(\hat{Z}/z_{mw}), \tag{5.9}$$

where the matched height is $z_{mw} = kz_0\exp(-\kappa c/u_{*w})$. Boundary conditions and equations governing perturbations to the flow in the water are then mapped to (5.4)–(5.7) if

$$\left.\begin{aligned} \Delta u_w &= \mathrm{Re}\{-U_{0w}\hat{u}(\hat{Z})k\hat{\eta}\}, \quad \Delta w_w = \mathrm{Re}\{-U_{0w}\hat{w}(\hat{Z})k\hat{\eta}\}, \\ \Delta p_w &= \mathrm{Re}\{\rho_w(U_{0w}^2\hat{\sigma}(\hat{Z}) - g'/k)k\hat{\eta}\}, \quad \Delta\tau_w = \mathrm{Re}\{\rho_w u_{*w}^2\hat{\tau}(\hat{Z})k\hat{\eta}\}, \end{aligned}\right\} \tag{5.10}$$

It is convenient to rewrite these relations such that the perturbations are proportional to $\eta(X,c)$, the same factor as in the air-flow perturbations. This is done by noting that $\hat{\eta}(\hat{X},\hat{c}) = -\eta^\dagger(X,c)$ (superscript $\dagger$ denotes complex conjugate) and using $\mathrm{Re}(A^\dagger) = \mathrm{Re}(A)$ for a complex number A. Perturbations in the water may then be written

$$\left.\begin{aligned} \Delta u_w &= \mathrm{Re}\{U_{0w}\hat{u}^\dagger(\hat{Z})k\eta\}, \quad \Delta w_w = \mathrm{Re}\{U_{0w}\hat{w}^\dagger(\hat{Z})k\eta\}, \\ \Delta p_w &= \mathrm{Re}\{-\rho_w(U_{0w}^2\hat{\sigma}^\dagger(\hat{Z}) + g'/k)k\eta\}, \quad \Delta\tau_w = \mathrm{Re}\{-\rho_w u_{*w}^2\hat{\tau}^\dagger(\hat{Z})k\eta\}, \end{aligned}\right\} \tag{5.11}$$

which also satisfy (5.4)–(5.7).

5.3. *Summary of method for solving the generic equations*

Hunt *et al.* (1988) have solved the generic equations (5.4)–(5.6) subject to the boundary conditions (5.7) for a stationary wave ($c = 0$), using the method of matched asymptotic expansions, and their solutions have been extended to higher order by Belcher *et al.* (1993). When the wave moves the equations are different because the unperturbed velocity profile is different and, if $c > 0$, there is a matched height at $Z = z_{ma}$ in the air. Belcher & Hunt (1993) analysed the flow in the vicinity of the matched height when the waves are slowly moving. Then z_{ma} is at the bottom of the inner region, close to the interface and the velocity perturbations at z_{ma} are small. Consequently, the flow above the matched height is the same as the flow over a stationary wave (with small corrections), but with a modified roughness length equal to z_{ma}. Here we also study the slow-wave limit and so solutions to the generic equations are quoted from Belcher & Hunt (1993) and used, with (5.2) and (5.11), to construct perturbations to the air and water flows. A brief outline of the asymptotic method is presented so that the solution can be fully interpreted.

5.3.1. *Outer region*

In the outer region the turbulent stress is changed by rapid distortion and, according to §4.3.1, when the waves are slowly moving the Reynolds-stress gradients are $O(\epsilon^2)$ smaller than the inertial terms and are negligible. Equations (5.4)–(5.6) can then be reduced to

$$\frac{\partial^2\hat{w}}{\partial\hat{Z}^2} - \left(1 + \frac{\hat{U}''}{\hat{U}}\right)\hat{w} = O(\epsilon). \tag{5.12}$$

Approximate solutions to (5.12) are constructed by dividing the outer region at the height where $|\hat{U}''/\hat{U}|$ equals one. In the air flow, $\hat{U}$ is typically logarithmic up to a height of $O(k^{-1})$ and $|\hat{U}''/\hat{U}|$ equals one at $\hat{Z} = \hat{h}$, where $\hat{h}\ln^{\frac{1}{2}}(\hat{h}/kz_m) = 1$. Using the definitions of U_0 and ϵ, this implies that

$$\hat{h} = (\epsilon/\kappa)^{\frac{1}{2}} \ll 1. \tag{5.13}$$

Conversely, if k^{-1} is much greater than the boundary-layer thickness, δ, then since there is no shear in the unperturbed velocity outside the boundary layer

$$\hat{h} = k\delta \ll 1. \tag{5.14}$$

This might be appropriate in the water flow.

In the upper layer, where $\hat{Z} \gg \hat{h}$, $\hat{U}''/\hat{U}$ is small and the perturbed flow is irrotational and inviscid. In the middle layer, where $\hat{Z} \ll \hat{h}$, $\hat{U}''/\hat{U}$ is large and the perturbations are inviscid but rotational. Pressure is constant across the middle layer at leading order and its value is determined by matching with the upper-layer solution at $\hat{Z} \sim \hat{h}$. A natural scale for velocity perturbations is therefore $U_{0\alpha} = \hat{U}(h)$, the unperturbed velocity evaluated at height h (where $\hat{h} = kh$). Velocity scales in the air and water are then

$$U_{0a} = (u_{*a}/\kappa)\ln(h_a/z_0) - c, \quad U_{0w} = (u_{*w}/\kappa)\ln(h_w/z_0) + c. \tag{5.15}$$

The different signs come from the different directions of the base flows in the air and water.

5.3.2. *Inner region*

The inner region is analysed by defining a scaled coordinate $\zeta = \hat{Z}/\hat{l} = O(1)$ where $\hat{l} = kl$ and l is defined in (4.3) or (4.5). The depth $\hat{l}$ can be related to ϵ by

$$\hat{l} = \frac{2\kappa}{S}\epsilon, \tag{5.16}$$

where $S = \hat{U}(\hat{l}) = 1 + O(\epsilon\ln(1/\epsilon))$ is the shear across the middle layer. The mixing-length model is used in the inner region, and, in dimensionless form, the perturbation shear-stress gradient is

$$\epsilon^2\frac{\partial\hat{\tau}}{\partial\hat{Z}} = S\frac{\partial}{\partial\zeta}\left(\zeta\frac{\partial\hat{u}}{\partial\zeta}\right) = O(1). \tag{5.17}$$

Hence the streamwise momentum equation becomes

$$\frac{\partial}{\partial\zeta}\left(\zeta\frac{\partial\hat{u}}{\partial\zeta}\right) - \mathrm{i}\hat{u} = \frac{\mathrm{i}\hat{\sigma}}{S} + \frac{\hat{w}}{2\kappa^2\zeta} + \frac{\epsilon}{\kappa S}\mathrm{i}\hat{u}\ln\zeta. \tag{5.18}$$

(The horizontal gradient of streamwise-velocity variance has been neglected—it affects the solution at only $O(\epsilon^2)$, Belcher *et al.* 1993.) Solutions are calculated iteratively in powers of ϵ.

Detailed analysis shows that the shear-stress gradient calculated using the above method diverges logarithmically towards the interface and it is necessary to analyse an even thinner, 'inner surface', layer (Sykes 1980). Across this layer the perturbation shear-stress gradient is approximately constant. Belcher & Hunt (1993) show that, when $kl_a/(2\kappa^2) \ll 1$, the matched height in the air flow lies within this layer and plays no role in the dynamics (because the effects of turbulent stresses are dominant in the inner surface layer). Hence Miles' (1957) critical-layer mechanism, which is an inviscid instability mechanism, cannot be effective in this parameter regime. In the water flow, for waves travelling with the wind, there is no matched height.

5.3.3. *Imaginary pressure coefficient*

Surface pressure perturbations that are out of phase with the irrotational flow produce a transfer of energy across the air–water interface and hence wave growth

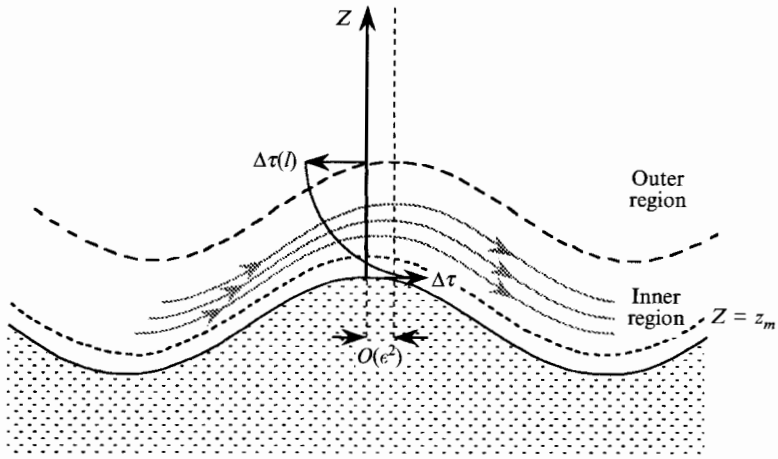

FIGURE 5. Schematic of non-separated sheltering. The perturbation shear-stress gradient decelerates the flow in the inner region and leads to streamlines in the outer region being displaced downwind of the wave crest.

or decay (see §5.5). In a normal mode analysis such an out-of-phase pressure is represented by an imaginary pressure coefficient.

Belcher *et al.* (1993) extended the Hunt *et al.* (1988) analysis and calculated the imaginary part of the pressure perturbation. A number of different physical processes can give rise to out-of-phase flow perturbations, but the dominant contribution to the asymmetric pressure comes from what Belcher *et al.* (1993) call *non-separated sheltering* and has the value

$$\mathrm{Im}(\hat{\sigma}) = -\frac{\mathrm{i}\epsilon^2}{S^2}\mathrm{Re}\{\hat{\tau}(\zeta \to \infty) - \hat{\tau}(0)\}. \tag{5.19}$$

Recall that the real part of the perturbation coefficient is the part that is observed at the crest of a sinusoidal wave. This expression has a simple physical explanation (refer to figure 5). Close to the surface, in the inner region, the real part of the perturbation to the shear-stress gradient is negative and decelerates the mean flow. The total deceleration in the inner region is the integral of the shear-stress gradient over the depth of the inner region, which is the change in shear stress across the inner region—the right-hand side of (5.19). Thus, streamlines at the top of the inner region are closer to the windward side of the wave than the leeward side. Flow in the outer region is then also asymmetrically displaced about the wave. However, according to RDT, shear-stress gradients are $O(\epsilon^2)$ in the outer region and there is no additional deceleration there (at leading order in ϵ). Hence, by Bernoulli, a pressure perturbation develops in the outer region that has its minimum displaced slightly downwind of the wave crest. This pressure is constant across the inner region (at leading order in ϵ) and so the surface pressure has an imaginary component. This is non-separated sheltering.

5.4. *Matching the shear stress at the interface*

Thus far we have set streamwise velocity at the interface to zero and simply computed the values of the shear stress either side of the interface: they are

$$\Delta\tau_a(0) = \rho_a u_{*a}^2 \mathrm{Re}\{\hat{\tau}_a(0)\, k\eta\}, \quad \Delta\tau_w(0) = -\rho_w u_{*w}^2 \mathrm{Re}\{[\hat{\tau}_w(0)]^\dagger\, k\eta\}. \tag{5.20}$$

The solution forced by the undulating interface is denoted with superscript (U); the solution derived using the methods of §5.3 by Belcher & Hunt (1993) is

$$\hat{\tau}_\alpha^{(U)}(0) = \frac{2}{S_\alpha^2}\left[1 + \frac{\epsilon_\alpha}{\kappa S_\alpha}\{1 + \mathrm{i}\pi + 4\gamma_E - \ln(z_{m\alpha}/z_0)\}\right] \equiv \frac{2}{S_\alpha^2}\left[1 + \epsilon_\alpha A_\alpha\right], \tag{5.21}$$

where subscript α denotes either air or water flows, $S_\alpha = U_\alpha(l_\alpha)/U_\alpha(h_\alpha)$ is the shear across the middle layer and $\gamma_E \approx 0.577$ is Euler's constant. The unperturbed shear stress is continuous (2.3) and so, if (5.21) is substituted into (5.20), then we find that the (U)-part of the shear-stress perturbation on either side of the interface has equal magnitude (with small corrections) but opposite sign.

But, according to the dynamical coupling condition (3.6), shear stress is constrained to be continuous at the interface. This stress imbalance can be corrected if we remember that the streamwise-velocity perturbation at the interface, $\Delta u(0)$, was set to zero in the calculation of the (U)-perturbations. If Δu is allowed to have a non-zero value at the surface, then further perturbations to the flow are produced; in particular, the surface shear stress is changed. The value of $\Delta u(0)$ is chosen such that shear stress is continuous at the interface.

As a consequence, if the flow in the water is assumed irrotational and inviscid, then it is not possible to satisfy the two boundary conditions that both velocity and stress are continuous at the interface: so there must be some sort of boundary layer in the water.

Changes to the boundary layer over a flat surface with a varying surface velocity are denoted by superscript (V). The (V)-perturbations are governed by the same equations as the (U)-perturbations, (3.10)–(3.12), but without the terms from the coordinate transformation. These equations are put into the standard form (5.4)–(5.6) using the scalings described in (5.2) and (5.11). Solutions to this problem have been found by Belcher, Xu & Hunt (1990) using methods similar to those described in §5.3. The governing equations are linear so the complete solution for flow over a wave with varying surface velocity is obtained by adding the (V)-perturbations to the (U)-perturbations (Belcher & Hunt 1993).

Figure 6 shows schematically how varying the surface-velocity perturbation can be used to satisfy stress continuity at the interface. Figure 6(*a*) shows the (U) velocity and shear-stress perturbations at the wave crest. Since the vertical gradient of $\Delta u_a^{(U)}$ is positive at the interface, $\Delta\tau_a^{(U)}(0)$ is also positive. Conversely, in the water, $\partial\Delta u_w^{(U)}/\partial Z$ is negative and so is the surface-shear-stress perturbation. Flow changes induced by a positive perturbation to surface velocity are sketched in figure 6(*b*). Gradients of perturbation velocity are positive and negative, respectively, above and below the interface, which gives rise to negative perturbations to the air-side shear stress and positive ones below the interface. The overall surface stress is made continuous by adding these two components, thereby decreasing the surface shear stress in the air and increasing it in the water.

On the air side $\Delta\hat{\tau}_a^{(V)}(0)$ scales on $\Delta u(0)/U_{0a}$ and $\Delta\hat{\tau}_w^{(V)}(0)$ on $\Delta u(0)/U_{0w}$. Since $U_{0a}/U_{0w} > 1$ and $\Delta u(0)$ is continuous, this implies that $\Delta\tau_w^{(V)}(0)$ is larger than $\Delta\tau_a^{(V)}(0)$. Hence, the resulting surface shear-stress perturbation is positive at the wave crest and close to $\Delta\tau_a^{(U)}(0)$.

If we write $\Delta u(0) = U_{0\alpha}\hat{u}_\alpha(0)\,k\eta$, then from Belcher & Hunt (1993) the surface shear stress induced by surface-velocity variation is

$$\hat{\tau}_\alpha^{(V)}(0) = -\frac{2\hat{u}_\alpha(0)}{S_\alpha}\left[1 + \frac{\epsilon_\alpha}{\kappa S_\alpha}\{\mathrm{i}\pi/2 + 2\gamma - \ln(z_{m\alpha}/z_0)\}\right] \equiv -\frac{2}{S_\alpha^2}\left[1 + \epsilon_\alpha B_\alpha\right]. \tag{5.22}$$

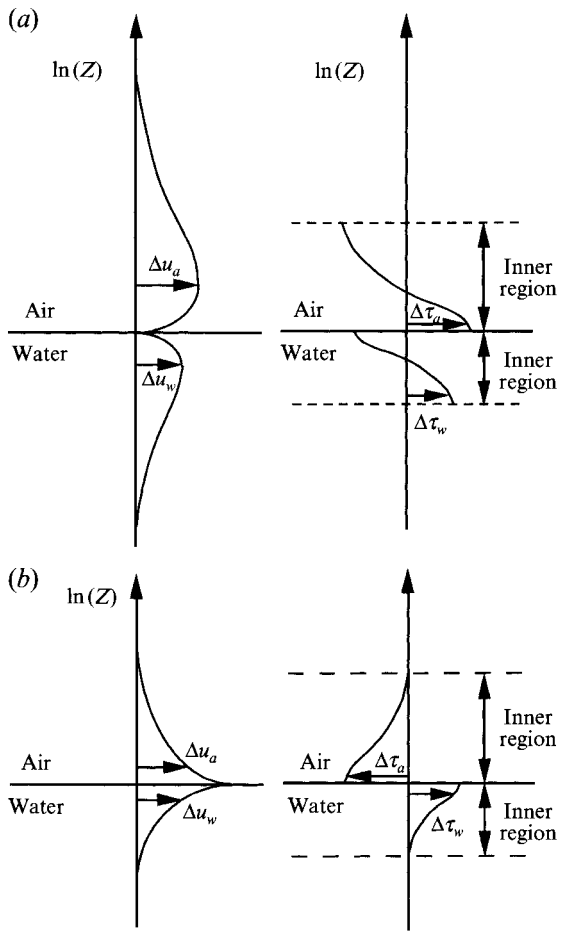

FIGURE 6. Matching the surface shear stress by varying the surface velocity: (*a*) schematic of (*U*)-perturbations at the wave crest; (*b*) schematic of (*V*)-perturbations at the wave crest.

Dimensional perturbations are obtained using (5.20).

Velocity is continuous at the interface, so that $\hat{u}_w(0) = \hat{u}_a(0)\, U_{0a}/U_{0w}$. The overall stress perturbation is given by $\hat{\tau}_\alpha = \hat{\tau}_\alpha^{(U)} + \hat{\tau}_\alpha^{(V)}$, so that the magnitude of the surface-velocity variation is determined by equating stress at each side of the interface. This implies that

$$\hat{u}_a(0)\left[\frac{1}{S_a}(1+\epsilon_a B_a)+\frac{1}{S_w}\frac{U_{0a}}{U_{0w}}(1+\epsilon_w B_w)\right] = \frac{1}{S_a^2}(1+\epsilon_a A_a)-\frac{1}{S_w^2}(1+\epsilon_w A_w). \quad (5.23)$$

A simplified form of this expression is developed in §6.2, where plots of the surface velocity are also shown.

5.5. *Determination of c*

According to the dynamical coupling condition, (3.6), normal stress, which is the sum of pressure and normal Reynolds stress, is continuous at the interface. First consider the normal Reynolds stress. In the inner region perturbations to the normal Reynolds stress are modelled as constant multiples of the shear stress perturbation, see (4.7). Hence, normal Reynolds stress is continuous across the interface because shear stress

is continous. Thus pressure is matched at the interface to determine the eigenvalue c, which gives the wave phase speed (real part of c) and growth rate (k times the imaginary part of c) of the wave.

The pressure perturbation just above the interface is

$$\Delta p_a(0) = \rho_a U_{0a}^2 \hat{\sigma}_a k\eta, \tag{5.24}$$

and just below it is

$$\Delta p_w(0) = -\rho_w U_{0w}^2 \left(\hat{\sigma}_w^{\dagger} + \frac{g'}{U_{0w}^2 k}\right) k\eta. \tag{5.25}$$

In the water, perturbation pressure is composed of a dynamic part, $-\rho_w U_{0w}^2 \hat{\sigma}_w$, and a hydrostatic part, $-\rho_w g'/k$. Furthermore, each pressure coefficient is composed of two parts: that induced by the wavy interface (denoted by superscript (U)) and that induced by the surface-velocity perturbation (denoted by superscript (V)). Solutions, from Belcher *et al.* (1993) and Belcher & Hunt (1993), for the undulation part are

$$\hat{\sigma}_a^{(U)} = -\left(1 - \frac{4\mathrm{i}\epsilon_a^2}{S_a^4}\right), \quad \left[\hat{\sigma}_w^{(U)}\right]^{\dagger} = -\left(1 + \frac{4\mathrm{i}\epsilon_w^2}{S_w^4}\right). \tag{5.26}$$

Solutions, from Belcher & Hunt (1993), for the streamwise-velocity variation part of the pressure perturbation are

$$\hat{\sigma}_a^{(V)} = -\frac{\Delta u(0)}{U_{0a}} \frac{2\mathrm{i}\epsilon_a^2}{S_a^3}, \quad \left[\hat{\sigma}_w^{(V)}\right]^{\dagger} = \frac{\Delta u(0)}{U_{0w}} \frac{2\mathrm{i}\epsilon_w^2}{S_w^3}. \tag{5.27}$$

These expressions show that the magnitude of the normalized pressure perturbation is one with corrections of $O(\epsilon_\alpha^2)$. Hence we write

$$\hat{\sigma}_a = \hat{\sigma}_a^{(U)} + \hat{\sigma}_a^{(V)} = -\mathrm{e}^{\mathrm{i}\Delta\phi_a}, \quad \hat{\sigma}_w^{\dagger} = \left[\hat{\sigma}_w^{(U)}\right]^{\dagger} + \left[\hat{\sigma}_w^{(V)}\right]^{\dagger} = -\mathrm{e}^{\mathrm{i}\Delta\phi_w}, \tag{5.28}$$

where the $\Delta\phi_\alpha$ are phase shifts of the pressure perturbations from the wave crests. $\Delta\phi_a$ is negative and so, in the air, the surface pressure minimum is shifted downwind of the wave crest; conversely, in the water, $\Delta\phi_w$ is positive and the surface pressure minimum is shifted upwind of the wave crest.

The velocity scales are rewritten as

$$U_{0a} = U_a - c, \quad U_{0w} = U_w + c, \tag{5.29}$$

where $U_\alpha = (u_{*\alpha}/\kappa)\ln(h_\alpha/z_0)$. Pressure is matched at the interface so that c is determined from

$$-\rho_a(U_a - c)^2 \mathrm{e}^{\mathrm{i}\Delta\phi_a} = \rho_w\{(U_w + c)^2 \mathrm{e}^{\mathrm{i}\Delta\phi_w} - g'/k\}. \tag{5.30}$$

Now write $\tilde{\rho}_a = \rho_a \mathrm{e}^{\mathrm{i}\Delta\phi_a}$, $\tilde{\rho}_w = \rho_w \mathrm{e}^{\mathrm{i}\Delta\phi_w}$ and $\tilde{g} = g'\mathrm{e}^{-\mathrm{i}\Delta\phi_w}$, and (5.30) reduces to the dispersion relation for a vortex sheet between two fluids of densities $\tilde{\rho}_a$ and $\tilde{\rho}_w$ and a gravitational acceleration $\tilde{g}$. If $c_0 = (g'/k)^{\frac{1}{2}}$ is the phase speed of a free-surface irrotational wave and $\tilde{c}_0 = (\tilde{g}/k)^{\frac{1}{2}}$, the solution to (5.30) can be written

$$c = \frac{\tilde{\rho}_a U_a - \tilde{\rho}_w U_w}{\tilde{\rho}_a + \tilde{\rho}_w} \pm \left\{\frac{\tilde{\rho}_w}{\tilde{\rho}_w + \tilde{\rho}_a}\tilde{c}_0^2 - \frac{\tilde{\rho}_a \tilde{\rho}_w}{(\tilde{\rho}_w + \tilde{\rho}_a)^2}(U_a + U_w)^2\right\}^{\frac{1}{2}}. \tag{5.31}$$

Capillary effects can be included by redefining c_0 as the wave speed for capillary–gravity waves using the formula given in Phillips (1977, p. 37). However, for such small wavelengths, the base flow used in the present analysis may not be appropriate. Capillary effects are not further discussed here.

6. Evaluation and interpretation of results

Solutions described in the preceding section cannot be evaluated immediately because the velocity and stress perturbations depend on c, which in turn depends on velocity scales, $U_{0\alpha}$. Hence, to obtain specific results, solutions are calculated iteratively. We have done this numerically. Firstly, the wave speed is approximated by c_0, the speed of irrotational waves. The scale heights of the inner regions in the air and water are then found using (4.3) and (4.5); the scale heights of the middle layers and the velocity scales, U_{0a} and U_{0w}, can then be evaluated (using (5.15)). The wave speed is then corrected using (5.31) and the procedure repeated. Convergence is achieved after three or four iterations. Once l_a, l_w and the wave speed are found, the surface velocity perturbation and growth rate of the wave are evaluated. These results, together with approximate formulae, are now presented.

6.1. *Wave phase speed*

The phase angles $\Delta\phi_\alpha$ are $O(\epsilon_\alpha^2)$, and so at leading order c is determined from (5.31) with $\tilde{\rho}_a$, $\tilde{\rho}_w$ and $\tilde{g}$ replaced by ρ_a, ρ_w and g', namely

$$c \sim \frac{\rho_a U_a - \rho_w U_w}{\rho_a + \rho_w} \pm \left\{ \frac{\rho_w}{\rho_w + \rho_a} c_0^2 - \frac{\rho_a \rho_w}{(\rho_w + \rho_a)^2} (U_a + U_w)^2 \right\}^{\frac{1}{2}} + O(\epsilon_\alpha^2 c_0). \tag{6.1}$$

This expression has imaginary solutions, corresponding to Kelvin–Helmholtz instability, if the term in the square root is negative, otherwise it is real and is the leading-order expression for the wave phase speed. The condition that the square root is negative reduces to

$$c_0/u_{*a} \lesssim (U_a/u_{*a})(\rho_a/\rho_w)^{\frac{1}{2}}, \tag{6.2}$$

because $U_a \gg U_w$ and the density ratio is small — for an air–water system $(\rho_a/\rho_w)^{\frac{1}{2}} \approx 1/30$. If typical numerical values are substituted, we find that Kelvin–Helmholtz instability requires small wave speeds and thus small wavelengths. For example, when kz_0 is between 10^{-5} and 10^{-7} and c_0/u_{*a} between 1 and 20, U_a/u_{*a} ranges from about 26 to 37, hence, Kelvin–Helmholtz instability occurs only when $c_0/u_{*a} \lesssim 1$. When $u_{*a} = 0.5\,\mathrm{m\,s^{-1}}$, Kelvin–Helmholtz instability then requires $\lambda \lesssim 0.1\,\mathrm{m}$. These small wavelengths are already excluded from our analysis because they require that capillary effects and the viscous sublayer in the base flows need to be considered. Hence, Kelvin–Helmholtz instability is not active in the parameter range we study.

When $c_0/u_{*a} \gtrsim 2$ (the exact value depends on kz_0), $(\rho_a/\rho_w)^{\frac{1}{2}}(U_a + U_w - c_0)/c_0$ is small and equation (6.1) can be approximated thus:

$$\mathrm{Re}(c) \sim \pm c_0 - U_w - \frac{1}{2}\frac{\rho_a}{\rho_w}\frac{(U_a + U_w \mp c_0)^2}{c_0} + O\left(\frac{\rho_a^2}{\rho_w^2}\right). \tag{6.3}$$

This expression for the wave speed is referred to a frame where the unperturbed velocity is zero at the interface (see figure 2). Changing to a frame where there is no flow at large depths in the water, the phase speed is $\mathrm{Re}(\tilde{c})$, given by

$$\mathrm{Re}(\tilde{c}) \sim U_s \pm c_0 - U_w + O(\rho_a/\rho_w), \tag{6.4}$$

where U_s is the surface drift in the frame of reference with no water motions far below the interface. For the remainder we focus on positive c_0, for waves moving with the wind.

Equation (6.4) shows how the wave speed depends on surface drift, U_s, and shear

in the water flow, through U_w. Surface drift is part of the base flow and so it is not part of our analytical solution, rather it must be specified beforehand (the numerical model described in Part 2 calculates the base flow and hence U_s). The value of U_w is determined by the scale height of the middle layer in the water, h_w, which is dependent on the depth of the wind-driven drift current and the wavelength (see §5.3.1). U_w lies between two extreme values. Firstly, in the absence of shear, $U_w = 0$ and waves are advected along with the current and have speed $c_0 + U_s$. Secondly, if the wavelength is longer than the depth of the sheared current, then h_w equals the boundary-layer depth and $U_w = U_s$. The waves are then so long that the inviscid motions they induce are unaffected by the wind-driven current and their speed is $c \approx c_0$. In summary, surface drift tends to increase wave speeds and shear in the drift current tends to decrease the wave speed; these qualitative findings are consistent with van Gastel *et al.* (1985), who considered gravity–capillary waves of small wavelength.

Experiments by Wu (1975) suggest that $U_s \approx 0.5u_{*a}$. Furthermore, U_w is of the order of U_s. The wave speed is therefore c_0 with corrections of $O(u_{*a})$. We consider values of $c_0/u_{*a} \gtrsim 1$ and so the $O(u_{*a})$ corrections to the wave speed are small relative to c_0. By contrast, van Gastel *et al.* (1985) considered small values of c_0/u_{*a} and hence found that $O(u_{*a})$ corrections to c_0 due to drift are important.

6.2. *Surface velocity variation*

The surface-velocity variation, which is given by (5.23), can be crudely approximated in the limit that ϵ_a and ϵ_w approach zero; we find

$$\frac{\Delta u_a(0)}{c_0} \sim \frac{3}{2 + c_0/U_{0a}}. \tag{6.5}$$

Hence, at leading order, the surface-velocity variation has a larger magnitude than if the flow in the water were inviscid and irrotational, when $\Delta u(0)/c_0 = 1$. Variation of surface-velocity perturbation (obtained from (5.23)) with c/u_{*a} is plotted in figure 7, which confirms the simple argument described in §5.4 that it is positive. Figure 7 also indicates the range of validity of the approximations: at large values of c/u_{*a}, the surface velocity becomes large indicating that the theory is no longer valid. Hence the approximations used in the theory require that $c/u_{*a} \lesssim 10$ when $kz_0 = 10^{-4}$, $c/u_{*a} \lesssim 13$ when $kz_0 = 10^{-5}$ and $c/u_{*a} \lesssim 16$ when $kz_0 = 10^{-6}$.

Variation of the surface shear stress with c/u_{*a} is shown in figure 8. Also shown is the shear stress when calculated from only the undulation part of the solution at the air and water sides of the interface. The argument of §5.4 is confirmed and the balanced stress is closer to $\Delta\tau_a^{(U)}(0)$.

6.3. *Wave growth rate*

The wave growth rate is $k\mathrm{Im}(c)$. With the condition that $(\rho_a/\rho_w)(U_a + U_w - c_0)^2/c_0^2 \ll 1$, (5.31) can be expanded by the binomial theorem, and the imaginary part of c is given by

$$\mathrm{Im}(c) \sim -c_0\frac{1}{2}\Delta\phi_w - \frac{1}{2}\frac{\rho_a}{\rho_w}\left\{(\Delta\phi_a - \frac{1}{2}\Delta\phi_w)\frac{(U_a + U_w - c_0)}{c_0} - \Delta\phi_w\right\}(U_a + U_w - c_0)$$
$$+ O\left(\frac{\rho_a^2}{\rho_w^2}\right). \tag{6.6}$$

Wave growth is therefore controlled by the phase of the dynamical pressure perturbations above and below the interface. Notice how the terms from the air flow

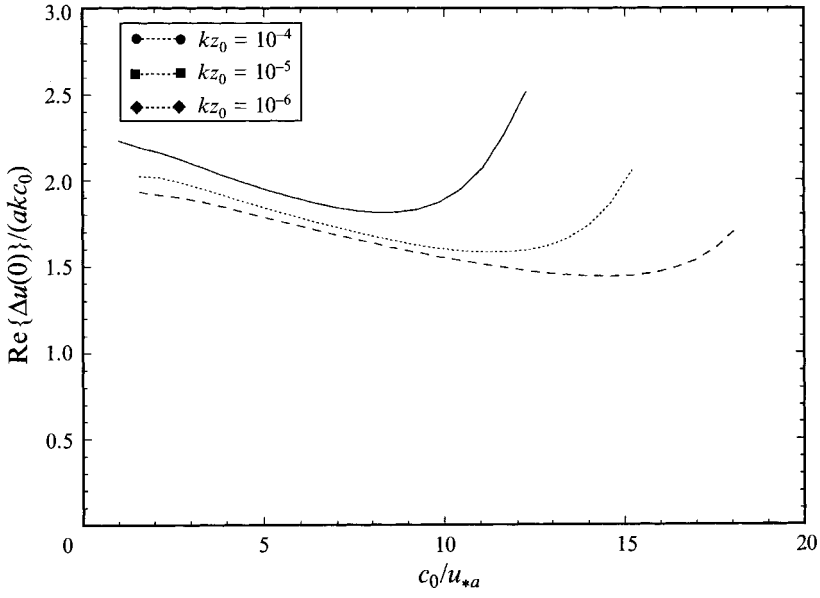

FIGURE 7. Surface velocity perturbation at the wave crest for various relative surface roughnesses.

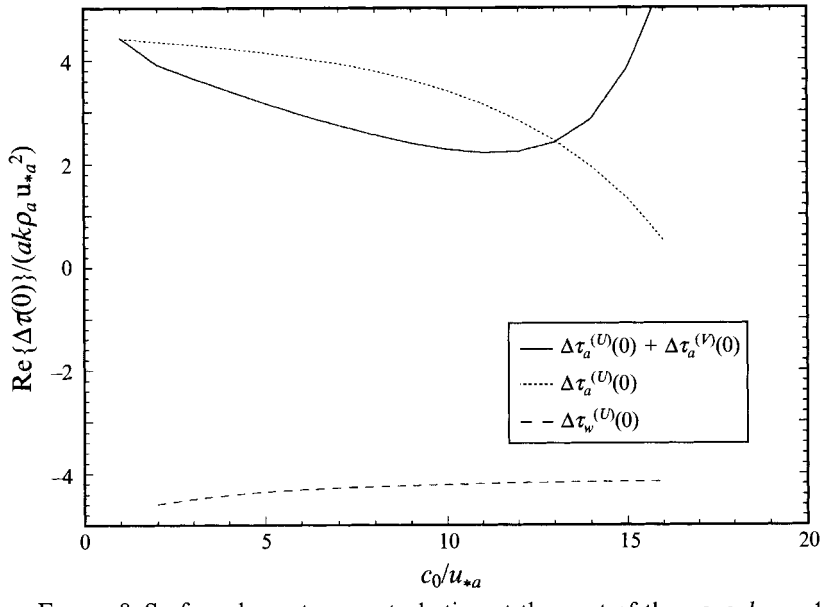

FIGURE 8. Surface shear-stress perturbation at the crest of the wave, $kz_0 = 10^{-5}$.

are multiplied by ρ_a/ρ_w, whereas the first term from the water flow is not. Since $\rho_a/\rho_w \approx 1/800$, this suggests that the evolution of the waves is sensitive to the flow in the water.

If the truncated mixing-length model is used, the imaginary part of the pressure in the water flow is $O(\rho_w u_{*w}^2)$ which is equal to $O(\rho_a u_{*a}^2)$, whereas the real part is $O(\rho_w(U_w + c)^2) = O(\rho_w c_0^2)$, using (6.3). The ratio of these gives the magnitude of the

pressure phase angle,

$$\Delta\phi_w = O((\rho_a/\rho_w)(u_{*a}^2/c_0^2)). \tag{6.7}$$

Hence, according to this model the effects of the drift current on wave growth are of the same order as the effects of the air flow. We will show that different turbulence models can change this magnitude.

Phase angles of the pressure computed using the truncated mixing-length model (4.7) are obtained from (5.26) and (5.27); they become, on using the approximation to Re(c),

$$\begin{aligned}\Delta\phi_a &= -2\epsilon_a^2\left(\frac{2}{S_a^4} - \frac{\Delta u(0)}{U_a - c}\frac{1}{S_a^3}\right)\\ &\sim -2\frac{u_{*a}^2}{(U_a + U_w - c_0)^2}\left(\frac{2}{S_a^4} - \frac{\Delta u(0)}{U_a + U_w - c_0}\frac{1}{S_a^3}\right) + O\left(\frac{\rho_a^2}{\rho_w^2}\right),\end{aligned} \tag{6.8}$$

$$\Delta\phi_w = 2\epsilon_w^2\left(\frac{2}{S_w^4} - \frac{\Delta u(0)}{U_w + c}\frac{1}{S_w^3}\right) \sim 2\frac{\rho_a}{\rho_w}\frac{u_{*a}^2}{c_0^2}\left(\frac{2}{S_w^4} - \frac{\Delta u(0)}{c_0}\frac{1}{S_w^3}\right) + O\left(\frac{\rho_a^2}{\rho_w^2}\right). \tag{6.9}$$

If (6.8) and (6.9) are substituted into (6.6), then the growth rate of the wave is given, in dimensionless form, by

$$\begin{aligned}\frac{\mathrm{Im}(c)}{c_0} \sim \frac{\rho_a}{\rho_w}\frac{u_{*a}^2}{c_0^2}&\left[\left\{\frac{2}{S_a^4} - \frac{2}{S_w^4}\right\} - \frac{\Delta u(0)}{c_0}\left\{\frac{c_0}{U_a + U_w - c_0}\frac{1}{S_a^3} - \frac{1}{S_w^3}\right\}\right]\\ &+ O\left(\frac{\rho_a^2}{\rho_w^2}\right).\end{aligned} \tag{6.10}$$

Figure 9(a–c) shows the variation of wave growth rate according to (6.10) with c/u_{*a}, for $kz_0 = 10^{-4}$, 10^{-5} and 10^{-6}. Also shown for comparison are growth rates obtained by assuming that the flow in the water is irrotational (obtained by setting $\Delta\phi_w = 0$ and $U_w = 0$ in (6.10)). If effects of the wind-driven current are included, then the growth rate is significantly reduced compared with values obtained from flow over irrotational waves. At large values of c/u_{*a}, the growth rate from the fully coupled model falls sharply to zero; in contrast, results from the irrotational-wave model remain approximately constant. Figure 9 also shows values for the growth rate obtained from the (U)-perturbations only (so that $\Delta u(0)$ is set to zero and the shear stress is discontinuous across the interface); this might show the maximum effect that the wind-induced current can have on wave growth. The growth rate obtained from only the (U)-perturbations is much smaller than from the fully coupled model, particularly at low wave speeds.

The differences between the fully coupled model and the irrotational-wave model are from two effects. Firstly, non-separated sheltering occurs in both the air and water flows, which leads to the surface pressure minimum being shifted from the wave crest by $\Delta\phi_a$ and $\Delta\phi_w$ in the air and water (see figure 10). In the air flow, $\Delta\phi_a$ is negative and the pressure minimum is shifted downwind of the crest, which promotes wave grow; whereas, $\Delta\phi_w$ is positive and the shift of the pressure minimum is upwind, which tends to inhibit wave growth. Hence, the Reynolds stress in the turbulent drift current, which leads to non-separated sheltering, tends to reduce the wave growth rate compared with flow over irrotational waves. The second effect of the wind-driven current on wave growth in our model arises from satisfying the boundary condition that shear stress is continuous at the interface. This condition has been satisfied by introducing the (V)-perturbations. Thence, $\Delta\tau_a^{(U)+(V)}(0)$ is reduced

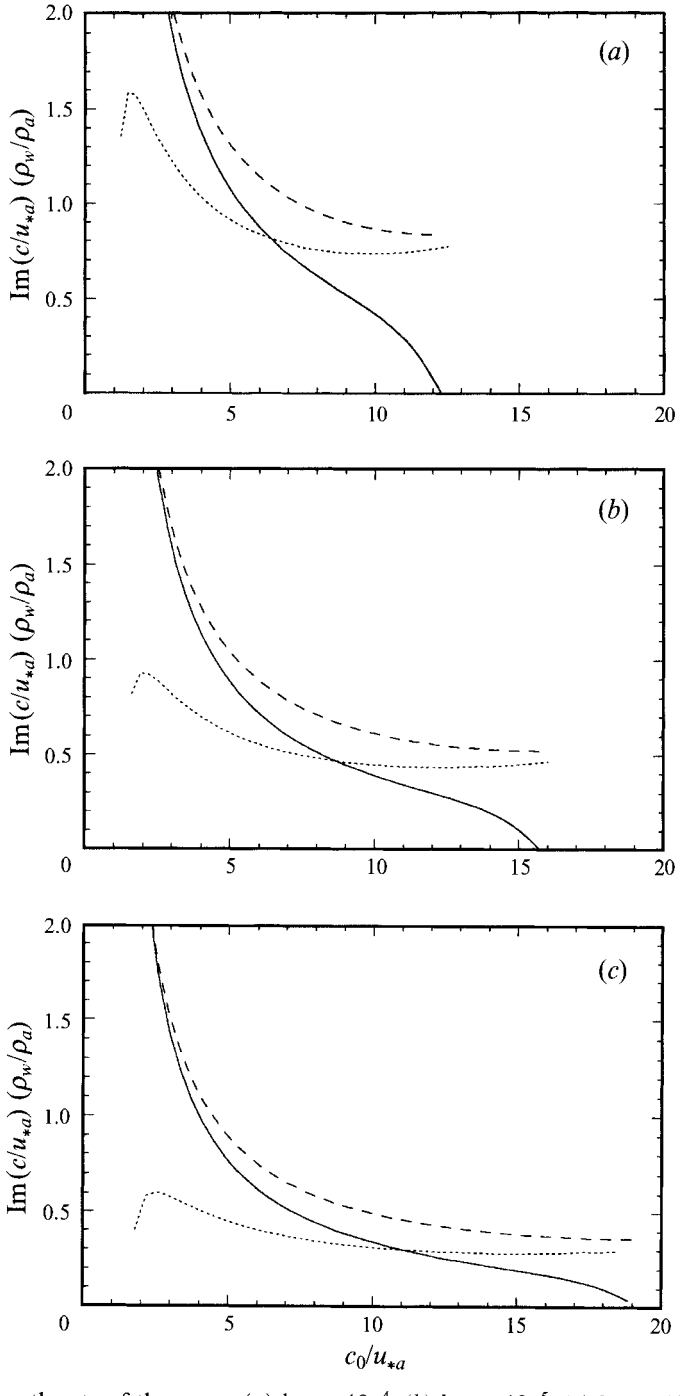

FIGURE 9. Growth rate of the wave: (*a*) $kz_0 = 10^{-4}$, (*b*) $kz_0 = 10^{-5}$, (*c*) $kz_0 = 10^{-6}$. Solid line, full theory; dotted line, (U)-perturbations only; dashed line, wave treated as irrotational.

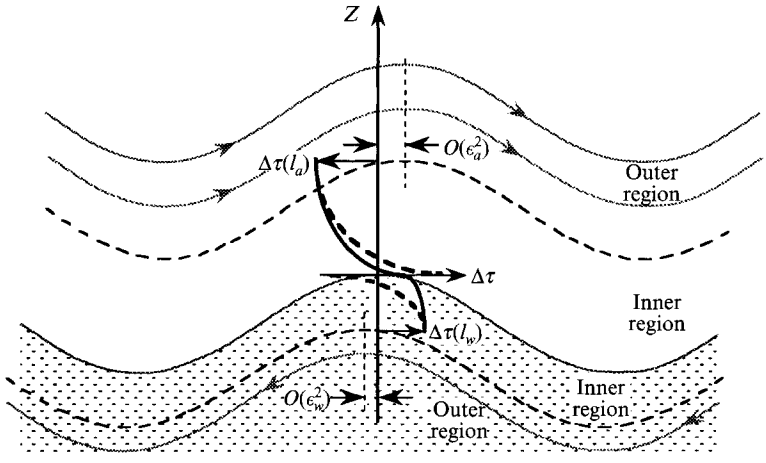

FIGURE 10. Schematic showing how coupling the air and water flows changes the wave growth rate. Profiles of the shear-stress perturbation at the wave crest are sketched: the dashed lines show the (U)-perturbations and the solid lines the profiles in the balanced state.

compared with $\Delta\tau_a^{(U)}(0)$; whereas, $\Delta\tau_w^{(U)+(V)}(0)$ is increased from $\Delta\tau_w^{(U)}(0)$, which is negative, to a positive value equal to $\Delta\tau_a^{(U)+(V)}(0)$ (see the sketch in figure 10). Non-separated sheltering, which is proportional to the change in shear stress across the inner region (see §5.3.3), is reduced in the air flow and so the wave growth rate is reduced. In the water flow the (V)-perturbations are of comparable magnitude to the (U)-perturbations, because $\Delta u(0)/c_0 = O(1)$, and the non-separated sheltering in the water is significantly reduced compared to the value obtained from only the (U)-perturbations.

In Part 3 we examine how turbulent motions in the water change the energy budget of the coupled flow, which provides further insight into and interpretation of (6.10).

7. Discussion and comparisons

Recently there have been a number of asymptotic studies of air flow over a wave that treated the flow in the water as inviscid and irrotational (Jacobs 1987; van Duin & Janssen 1992; Belcher & Hunt 1993). These studies are all based on the same approximations, namely that $\epsilon \to 0$ with c/u_{*a} fixed and of order one, but reached different conclusions so it is interesting to compare their results to reconcile the differences.

Van Duin & Janssen (1992) used a general eddy-viscosity model for the turbulent shear stress, namely $\Delta\tau = \nu_t \partial\Delta u/\partial Z$, throughout the flow. Their choice of eddy viscosity was

$$\nu_t = \ell^{1+n} u_*^{1-n} \left| \frac{\partial u}{\partial Z} \right|^n, \tag{7.1}$$

where the mixing length is $\ell = \kappa Z$. This model reduces to Jacobs' (1987) form if $n = 0$ and to the standard mixing length if $n = 1$. Van Duin & Janssen (1992) worked with the stream function of the perturbed flow and found that in the outer region it is

$$\Psi \sim ak\{1 - c/U_B(k^{-1})\} \left[e^{-\hat{Z}} + \epsilon_1 \left\{-\frac{1}{\kappa}(\gamma + \ln 2)e^{-\hat{Z}} - \frac{1}{\kappa}e^{\hat{Z}}E_1(2\hat{Z}) + \tfrac{1}{2}in\kappa(\hat{Z}^2 - \hat{Z})e^{-\hat{Z}}\right\}\right] + \cdots, \quad (7.2)$$

where E_1 is an exponential function and the small parameter is $\epsilon_1 = u_{*a}/(U_B(k^{-1}) - c_0)$, which is of $O(\epsilon_a)$. They then obtained an expression for the pressure perturbation at the interface. Using their results, the phase shift of the pressure minimum from the wave crest can be calculated (as in §5.5); in the present notation it is

$$\Delta\phi_{VDJ} = -2\kappa\epsilon_1(1 + \tfrac{1}{4}n)\frac{U_B(k^{-1})}{U_B(k^{-1}) - c_0}. \quad (7.3)$$

$\Delta\phi_{VDJ}$ is bigger by a factor $O(1/\epsilon_a)$ than the value used here, $\Delta\phi_a$, obtained by Belcher *et al.* (1993) and Belcher & Hunt (1993) with the truncated mixing-length model. When $\Delta u(0) = 0$ our value is

$$\Delta\phi_a = -4\epsilon_a^2/S_a^4. \quad (7.4)$$

Before presenting quantitative comparisons of these models, (7.3) is extended heuristically to provide an expression that is correct to $O(\epsilon_a^2)$ for the surface-pressure phase obtained using the mixing-length model throughout the flow. Firstly, there are second-order terms generated in the outer region. These terms can be estimated on observing that (7.2) contains an $O(\epsilon_1)$ term that decays exponentially with height. If this term is grouped with the $O(1)$ exponential, then, following the analysis of van Duin & Janssen (1992), the imaginary term in (7.2) becomes multiplied by a factor of $\{1 - (\gamma + \ln 2)\epsilon_1/\kappa\}$, and thence so is the imaginary part of the surface pressure. Secondly, as Wood & Mason (1993) recognized, these outer-region terms must be added to the contribution from non-separated sheltering in the inner region (7.4). Overall then, the pressure phase from using mixing length throughout the flow from this heuristic procedure is

$$\Delta\phi_{ML} = -\tfrac{5}{2}\epsilon_1\kappa\{1 - (\gamma + \ln 2)\epsilon_1/\kappa\} - 4\epsilon_a^2/S_a^4. \quad (7.5)$$

There is a physical interpretation of this procedure. The pressure phase in (7.3) is from a sheltering effect in the outer region, i.e. interaction in the outer region between inertial terms and the spuriously large shear-stress gradient obtained using mixing length in the outer region. This is in addition to the non-separated sheltering in the inner region and so, since the analysis is linear, the two effects must be added to obtain the total phase shift from using mixing length throughout the flow. The arguments of §4 demonstrate that use of mixing length in the outer region does not correctly represent the physical processes and will not agree with experimental data.

Figure 11 shows comparisons of these various formulae when they are used to compute drag on sinusoidal terrain, which is given by

$$\Delta F = -\rho_a u_{*a}^2 a^2 k\,\pi\Delta\phi/\epsilon_a^2. \quad (7.6)$$

Results of experiment and calculations based on turbulence models that relax to rapid distortion in the outer region are shown as filled symbols in figure 11, whereas, calculations based on an eddy viscosity in the outer region are shown as open symbols. Figure 11 clearly shows that the Belcher *et al.* (1993) formula, (7.4), is in good agreement with the experimental value and results of computations that use a full Reynolds stress model. The van Duin & Janssen formula (with $n = 1$), however, is neither in good agreement with numerical computations that use a mixing length throughout the flow nor with the Reynolds stress model. But when it is corrected

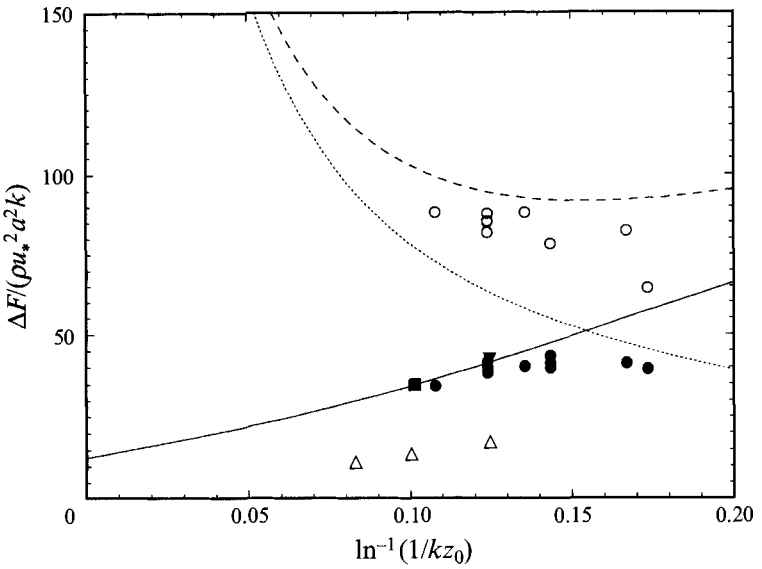

FIGURE 11. Force on a rigid sinusoidal wave (a hill). Theory: —, truncated mixing length (7.4); – – –, mixing length throughout, (7.5); - - - -, van Duin & Janssen, (7.3). Numerical model: •, Belcher *et al.* (1993) second-order closure; ○, Belcher *et al.* (1993) mixing-length closure; △, Townsend (1972); ▼, Townsend (1980). Experiment: ■, Zilker & Hanratty (1979)

by adding the contribution from non-separated sheltering, giving (7.5), the agreement with the mixing-length computations is reasonable, although they are up to a factor of two greater than values obtained with (7.4) and the experimental value. We acknowledge that, formally, for (7.5) to be an asymptotic expansion, the second term should be much smaller than the first. However, (7.5) agrees with the numerical model even when the two terms are comparable. It is clear from (7.5) that using other eddy-viscosity models in the outer region (i.e. different values of n) will also give drag coefficients that are too large. We believe that figure 11 provides compelling evidence that it is inappropriate to use the mixing-length model in the outer region. Furthermore, it provides strong evidence that the analytical approach used here with the truncated mixing length, which leads to (7.4), gives reliable values for the pressure phase shift.

7.1. *Wave growth rate calculated using mixing length throughout*

It is interesting and instructive to calculate the growth rate of the wave if the mixing-length model is used throughout the flow.

The phases of the pressure perturbations are given by

$$\left.\begin{aligned}\Delta\phi_a &= -\tfrac{5}{2}\epsilon_{1a}\kappa\{1-(\gamma+\ln 2)\epsilon_{1a}/\kappa\}-4\epsilon_a^2/S_a^4,\\ \Delta\phi_w &= \tfrac{5}{2}\epsilon_{1w}\kappa\{1-(\gamma+\ln 2)\epsilon_{1w}/\kappa\}+4\epsilon_w^2/S_w^4.\end{aligned}\right\} \tag{7.7}$$

The growth rate then becomes

$$\frac{\mathrm{Im}(c)}{c_0} \sim -\tfrac{5}{4}\kappa\left(\frac{\rho_a}{\rho_w}\right)^{\frac{1}{2}}\{1-(\gamma+\ln 2)\epsilon_{1w}/\kappa\} + \tfrac{5}{4}\kappa\frac{\rho_a}{\rho_w}\frac{U_a+U_w-c_0}{c_0}\{1-(\gamma+\ln 2)\epsilon_{1a}/\kappa\} + \text{terms from (6.10).} \tag{7.8}$$

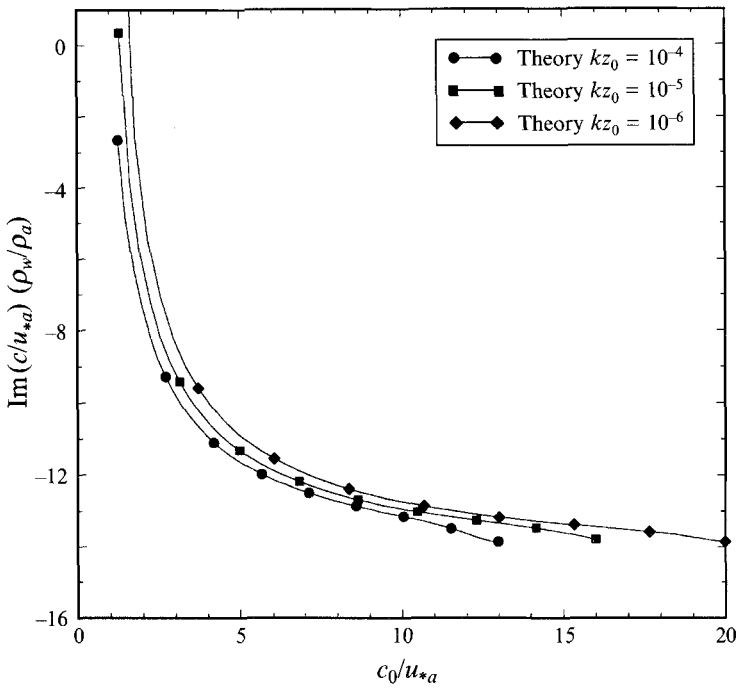

FIGURE 12. Growth rate of the wave; results computed using the mixing length throughout the flow.

Hence, if the mixing-length model is erroneously used throughout the flow, then the effect of sheltering in the outer region of the water motions induces a contribution to wave growth that scales as $(\rho_a/\rho_w)^{\frac{1}{2}}$, whereas, according to the truncated mixing-length model, non-separated sheltering in the water scales as ρ_a/ρ_w. Hence the growth is incorrectly dominated by sheltering in the outer region of the water flow. Figure 12, which shows the variation of (7.8) with c/u_{*a}, demonstrates that using mixing length throughout the flow leads to negative wave growth rates for all c/u_{*a}. Furthermore, the magnitude of these damping rates is about twenty times the growth rates obtained with the truncated mixing length and plotted in figure 9. According to the mixing length model, there are no waves on the ocean! This ridiculous conclusion provides more evidence that it is incorrect to use mixing length throughout the flow, particularly in the water.

8. Summary

Theoretical scaling and analysis have been developed to describe coupled air–water boundary-layer flow with a wavy interface. It has been shown that the unperturbed surface stress exerted by wind at the interface leads to a sheared drift current in the water, which previous laboratory experiments show to be turbulent at even low wind speeds. We have modelled these turbulent water motions in our analysis.

Scaling arguments, borrowed from flow over hills and extended, show how perturbations to the turbulence has a two-layer structure. Close to the surface, in the inner region of depth scale l_a, the turbulence is close to local equilibrium and eddy-viscosity models can be used. In an outer region, far above the inner, turbulence is

changed by rapid distortion and eddy-viscosity models are inappropriate. Using this division, the flow has been characterized in terms of the ratio $kl_a/(2\kappa^2)$. For slow waves $kl_a/(2\kappa^2) \lesssim \frac{1}{2}$ and the inner region is a thin layer close to the surface. When $kl_a/(2\kappa^2) \gtrsim 1$ the waves are fast and the inner region is thick and eddy-viscosity models are appropriate over the whole significant flow domain. Between these limits more sophisticated models are required. For waves travelling with the wind, the water flow has a narrow inner region for all wave speeds.

The analytical model for slow waves is based on three approximations: small wave slope, $ak \ll 1$; thin inner region, $kl_a/(2\kappa^2) = \epsilon_a/S_a \ll 1$, where $\epsilon_a = u_{*a}/U_{0a}$; and an inner region that lies well within the unperturbed boundary layer. Solutions for perturbations to the air and water motions are based on those of Belcher & Hunt (1993), who made extensive use of solutions for flow over a fixed wavy surface (a hill) found by Hunt *et al.* (1988) and Belcher *et al.* (1993). Perturbations to the flow induced by the undulating wave shape do not have continuous stress at the interface and a second component of the solution induced by a varying velocity at the surface is required to balance surface stress.

Pressure is matched at the interface to determine wave phase speed and growth rate. The phase speed is close to the value for irrotational free surface waves. Wave growth is determined by the phase of the dynamic pressure perturbations either side of the interface. The pressure phase shift in the air flow leads to a contribution to wave growth that is scaled down by the ratio of the fluid densities (ρ_a/ρ_w), whereas the phase shift in the water leads directly to a contribution to $\mathrm{Im}(c)$. Hence, there is extreme sensitivity of wave growth to motions in the water and the coupling conditions at the interface. We imposed the boundary condition that stress is continuous across the interface.

According to our calculations of the coupled flow with the truncated-mixing-length model, wave growth is reduced by a factor of about two compared with calculations based on flow over an irrotational wave. This reduction arises from two distinct mechanisms. Firstly, perturbations to the wind-driven drift current are asymmetrically displaced about the wave by non-separated sheltering. This sheltering leads to a pressure perturbation that is in phase with the wave slope and wave growth is inhibited. We have performed calculations using a mixing-length model throughout the flow that show how the model for the turbulent shear stress in the water has a large influence on this mechanism for wave damping. Secondly, there are perturbations to the air flow that arise from imposing the boundary condition that stress is continuous across the interface. The non-separated sheltering effect in the air is reduced by these motions and therefore the tendency for the wind to promote wave growth is reduced.

Perhaps the most interesting questions that arise from this study relate to the role played by the wind-induced drift current in the energy budget of the wind–wave interaction. How is energy transfer from wind to waves influenced by turbulent motions in the water? Which motions in the water are promoted by this energy transfer? How much energy from the wind increases wave energy and how much is dissipated in the water? What are the mechanisms for energy dissipation in the water motions? These are some of the issues we investigate in Parts 2 and 3 of our study. In Part 2, we describe a numerical model of the coupled flow and present comparisons of velocity and shear-stress profiles with the theory of this paper and experimental data. From these comparisons we suggest quantities that need to be modelled correctly to capture features such as wave growth. In Part 3 we investigate the energy budget for

the coupled flow. Expressions for the wave-induced perturbations from the theoretical and numerical models are used to evaluate the terms in this budget. The results are used to make further comparisons of our models with experimental measurements and to suggest improvements to wave-forecasting models.

It is a pleasure to acknowledge the helpful conversations we have had with Professor Julian Hunt in the course of this work. S.E.B. gratefully acknowledges the financial support of the Natural Environment Research Council under grant GR3/7886. S.E.B. thanks the staff and students of EFML, Stanford University for making him so welcome during two visits and is grateful for the financial support given for these visits through R.L.S. by Stanford University unrestricted research funds. J.A.H. and R.L.S. gratefully acknowledge the support of the Fluid Dynamics Program, Mechanics Division, Office of Naval Research, USA, under Grants N00014-90-J-1294 and N00014-91-J-1200 and Contract N00014-84-K-0242 for the work done at Stanford University. Research support for J.A.H. at the University of Melbourne has been provided by the G.K. Williams Cooperative Research Centre in the department of Chemical Engineering.

REFERENCES

AL-ZANAIDI, M. A. & HUI, W. H. 1984 Turbulent air flow over water waves – a numerical study. *J. Fluid Mech.* **148**, 225–246.

BANNER, M. L. & PEREGRINE, D. H. 1993 Wave breaking in deep water. *Ann. Rev. Fluid Mech.* **25**, 373–397.

BELCHER, S. E., HARRIS, J. A. & STREET, R. L. 1994 Linear dynamics of turbulent air–water flow with a wavy interface. Part 3. Energy budget. *J. Fluid Mech.* (Submitted)

BELCHER, S. E. & HUNT, J. C. R. 1993 Turbulent shear flow over slowly moving waves. *J. Fluid Mech.* **251**, 109-148.

BELCHER, S. E., NEWLEY, T. M. J. & HUNT, J. C. R. 1993 The drag on an undulating surface due to the flow of a turbulent boundary layer. *J. Fluid Mech.* **249**, 557–596.

BELCHER, S. E., XU, D. P. & HUNT, J. C. R. 1990 The response of a turbulent boundary layer to arbitrarily distributed two-dimensional roughness changes. *Q. J. R. Met. Soc.* **116**, 611–635.

BENJAMIN, T. B. 1959 Shearing flow over a wavy boundary. *J. Fluid Mech.* **6**, 161–205.

CHEUNG, T. K. & STREET, R. L. 1988 The turbulent layer in the water at an air–water interface. *J. Fluid Mech.* **194**, 133–151.

DAVIS, R. E. 1972 On prediction of turbulent flow over a wavy boundary. *J. Fluid Mech.* **52**, 287–306.

DONELAN, M. A. & HUI, W. H. 1990 Mechanics of ocean surface waves. In *Surface Waves and Fluxes* (ed. G.L. Geernaert & W.J. Plant), pp. 209–246. Kluwer.

DUIN, C. A. VAN & JANSSEN, P. A. E. M. 1992 An analytical model of the generation of surface waves by turbulent air flow. *J. Fluid Mech.* **236**, 197–215.

DURBIN, P. A. 1993 A Reynolds stress model for near-wall turbulence. *J. Fluid Mech.* **249**, 465–498.

GASTEL, K. VAN, JANSSEN, P. A. E. M. & KOMEN, G. J. 1985 On phase velocity and growth rate of wind-induced capillary–gravity waves. *J. Fluid Mech.* **161**, 199–216.

GENT, P. R. & TAYLOR, P. A. 1976 A numerical model of air-flow above water waves. *J. Fluid Mech.* **77**, 105–128.

HARRIS, J. A., BELCHER, S. E. & STREET, R. L. 1994 Linear dynamics of turbulent air–water flow with a wavy interface. Part 2. Numerical model. *J. Fluid Mech.* (Submitted)

HASSELMANN, D. & BÖSENBERG, J. 1991 Field measurements of wave-induced pressure over wind-sea and swell. *J. Fluid Mech.* **230**, 391–428.

HASSELMANN, K. 1962 On the nonlinear energy transfer in a gravity wave spectrum. Part 1. *J. Fluid Mech.* **12**, 481–500.

HSU, C. T. & HSU, E. Y. 1983 On the structure of turbulent flow over a progressive water wave: theory and experiement in a transformed, wave-following co-ordinate system. Part 2. *J. Fluid Mech.* **131**, 123–153.

HSU, C.T., HSU, E.Y. & STREET, R.L. 1981 On the structure of turbulent flow over a progressive water wave: theory and experiement in a transformed, wave-following co-ordinate system. *J. Fluid Mech.* **105**, 87–117.

HUNT, J.C.R., LEIBOVICH, S. & RICHARDS, K.J. 1988 Turbulent shear flows over low hills. *Q. J. R. Met. Soc.* **114**, 1435-1471.

JACOBS, S.J. 1987 An asymptotic theory for the turbulent flow over a progressive wave. *J. Fluid Mech.* **174**, 69–80.

JENKINS, A.D. 1987 Wind and wave induced currents in a rotating sea with depth-varying eddy viscosity *J. Phys. Oceanogr.* **17**, 938–951.

KONDO, J. 1976 Parameterization of turbulent transport in the top meter of the ocean. *J. Phys. Oceanogr.* **6**, 712–720.

KOMORI, S., NAGAOSO, R. & MURAKAMI, Y. 1993 Turbulence structure and mass transfer across a sheared air–water interface in wind-driven turbulence. *J. Fluid Mech.* **249**, 161–183.

LARSON, T.R. & WRIGHT, J.W. 1975 Wind-generated gravity-capillary waves: Laboratory measurements of temporal growth rates using microwave backscatter. *J. Fluid Mech.* **70**, 417–436.

MILES, J.W. 1957 On the generation of surface waves by shear flows. *J. Fluid Mech.* **3**, 185–204.

PHILLIPS, O.M. 1960 On the dynamics of unsteady gravity waves of finite amplitude. Part 1. *J. Fluid Mech.* **9**, 193–217.

PHILLIPS, O.M. 1977 *The Dynamics of the Upper Ocean*. Cambridge University Press.

PLANT, W.J. 1984 A relationship between wind shear stress and wave slope. *J. Geophys. Res.* **87**, C3, 1961–1967.

SHEMDIN, O.H. & HSU, E.Y. 1967 Direct measurement of aerodynamic pressure above a simple progressive gravity wave. *J. Fluid Mech.* **30**, 403–416.

SNYDER, R.L., DOBSON, F.W., ELLIOT, J.A. & LONG, R.B. 1981 Array measurements of atmospheric pressure fluctuations above gravity waves. *J. Fluid Mech.* **102**, 1–59.

SYKES, R.I. 1980 An asymptotic theory of incompressible turbulent flow over a small hump. *J. Fluid Mech.* **101**, 647–670.

TENNEKES, H. & LUMLEY, J.L. 1972 *A First Course in Turbulence*. MIT Press.

TOWNSEND, A.A. 1972 Flow in a deep turbulent boundary layer over a surface distorted by water waves. *J. Fluid Mech.* **55**, 719–735.

TOWNSEND, A.A. 1976 *Structure of Turbulent Shear Flow*. Cambridge University Press.

TOWNSEND, A.A. 1980 Sheared turbulence and additional distortion. *J. Fluid Mech.* **98**, 171–191.

URSELL, F. 1956 Wave generation by wind. In *Surveys in Mechanics* (ed. G.K. Batchelor & R.M. Davis), pp. 216–249. Cambridge University Press.

VALENZUELA, G.R. 1976 The growth of capillary–gravity waves in a coupled shear flow. *J. Fluid Mech.* **76**, 229–250.

WAMDI GROUP 1988 The WAM model—a third generation ocean wave prediction model. *J. Phys. Oceanogr.* **18**, 1775–1810.

WEBER, J.E. & MELSOM, A. 1993 Transient ocean currents induced by wind and growing waves. *J. Phys. Oceanogr.* **23**, 193–206.

WEST, B.J., BRUECKNER, K.A., JANDA, R.S., MILDER, D.M. & MILTON, R.L. 1987 A new numerical model for surface hydrodynamics. *J. Geophys. Res.* **92**, C11, 11803–11824.

WOOD, N. & MASON, P.J. 1993 The pressure force induced by neutral turbulent flow over hills. *Q. J. R. Met. Soc.* **119**, 1233–1267.

WU, H.Y., HSU, E.Y. & STREET, R.L. 1977 The energy transfer due to air-input, non-linear wave–wave interaction and white-cap dissipation associated with wind-generated waves. *Tech. Rep.* 207, pp. 1–158. Stanford University.

WU, H.Y., HSU, E.Y. & STREET, R.L. 1979 Experimental study of nonlinear wave–wave interaction and white-cap dissipation of wind-generated waves. *Dyn. Atmos. Oceans* **3**, 55–78.

WU, J. 1975 Wind-induced drift currents. *J. Fluid Mech.* **68**, 49–70.

ZEMAN, O. 1981 Progress in the modelling of planetary boundary layers. *Ann. Rev. Fluid Mech.* **13**, 253–272.

ZILKER, D.P. & HANRATTY, T.J. 1979 Influence of the amplitude of a solid wavy wall on a turbulent flow. Part 2. Separated flows *J. Fluid Mech.* **90**, 257–271.